Materials Today Bio 29 (2024) 101311

Contents lists available at ScienceDirect

Materials Today Bio

journal homepage: www.journals.elsevier.com/materials-today-bio

PH-sensitive adriamycin hydrochloride and oxaliplatin dual-loaded microspheres synergistically enhance local injections effect of hepatocellular carcinoma

Jialu Weng [a,1], Shiyi Wu [a,1], Yating Pan [a], Yifan Lai [a], Jinrong Zhu [c], Wenzhang Jin [e], Deyu Lu [a], Yizhang Chen [d], Zhijie Yu [h,***], Xinjie Zan [a,b,**], Jinglin Xia [a,f,g,*]

[a] Zhejiang Key Laboratory of Intelligent Cancer Biomarker Discovery and Translation, First Affiliated Hospital, Wenzhou Medical University, Wenzhou 325035, China
[b] Wenzhou Institute, Wenzhou Key Laboratory of Perioperative Medicine, University of Chinese Academy of Sciences, Wenzhou, 325000, China
[c] The Second School of Medicine Wenzhou Medical University, Wenzhou, 325000,China
[d] School of Pharmaceutical Sciences, Wenzhou Medical University, Wenzhou, Zhejiang, 325000, China
[e] Department of Colorectal Surgery, The Second Affiliated Hospital of Zhejiang Chinese Medical University, Hangzhou 310000, China
[f] Liver Cancer Institute, Zhongshan Hospital of Fudan University, Shanghai, 200032, China
[g] National Clinical Research Center for Interventional Medicine, Shanghai, 200032, China
[h] Wenzhou Key Laboratory of Hematology, The First Afliated Hospital of Wenzhou Medical University, Wenzhou 325000, Zhejiang, China

ARTICLE INFO

Keywords:
pH-sensitive nanoparticles
Drug-carrying microspheres
Adriamycin hydrochloride
Oxaliplatin
Local injection therapy
Liver cancer

ABSTRACT

Chemotherapy is the primary palliative treatment for advanced hepatocellular carcinoma (HCC). However, the systemic delivery is associated with the drawbacks including a high risk of adverse effects and a low efficacy. Therefore, local injection therapy may be beneficial. Nevertheless, the existing local drug-carrying microspheres (DOBM)have the characteristics of low loading and abrupt release, can not simultaneously load two drugs, and may cause unnecessary toxicity. In this study, we created the dual-loaded bovine serum albumin (BSA) microspheres (also known as DOBM), which were hollow and contained both oxaliplatin (OXA) and Adriamycin hydrochloride (DOX). In addition, this pH-sensitive drug delivery method exhibited a high drug loading capacity and was promising in breaking through biological barriers, making it a viable option for the treatment of HCC through local implantation. Based on physiochemical evaluation of BSA microspheres, they had a porous structure which was close to the surface. Adriamycin and oxaliplatin were successfully added to the surface of BSA microspheres. According to in vitro experimental results, the growth of human HCC (HCC-LM3 and PLC/PRF/5) cell lines was significantly inhibited by DOBM. Furthermore, in the subcutaneous PLC/PRF/5 HCC model, DOBM played an essential role in tumor development and change in the tumor microenvironment.

1. Introduction

Hepatocellular carcinoma (HCC) ranks the sixth among cancers in terms of its morbidity; besides, it also ranks the third among factors inducing cancer-related mortality worldwide [1]. HCC, which is frequently associated with chronic liver disease, is classified based on the cell origin of the tumor. It exhibits the highest prevalence, and originates from liver cells, occupying 75–85 % of all cases [2]. According to the HCC tumor stage and the degree of associated liver dysfunction, a variety of treatment options are available. Localized destructive treatment, surgery, and liver transplantation are among the therapeutic options benefiting patients with early-stage HCC [3]. Unfortunately, only approximately one-third of newly diagnosed HCC patients are suitable for these curative treatments. However, the 5-year recurrence rate of

* Corresponding author. Zhejiang Key Laboratory of Intelligent Cancer Biomarker Discovery and Translation, First Affiliated Hospital, Wenzhou Medical University, Wenzhou 325035, China.
** Corresponding author. Key Laboratory of Diagnosis and Treatment of Severe Hepato-Pancreatic Diseases of Zhejiang Province, The First Affiliated Hospital of Wenzhou Medical University, Wenzhou, 325000, Zhejiang, China.
*** Corresponding author. Wenzhou Key Laboratory of Hematology, The First Afliated Hospital of Wenzhou Medical University, Wenzhou 325000, Zhejiang, China.
E-mail addresses: zhijie_yu@wzhospital.cn (Z. Yu), zanxj@ucas.ac.cn (X. Zan), xiajinglin@fudan.edu.cn (J. Xia).
[1] Note: They contributed equally to this work.

https://doi.org/10.1016/j.mtbio.2024.101311
Received 18 June 2024; Received in revised form 22 September 2024; Accepted 24 October 2024
Available online 25 October 2024

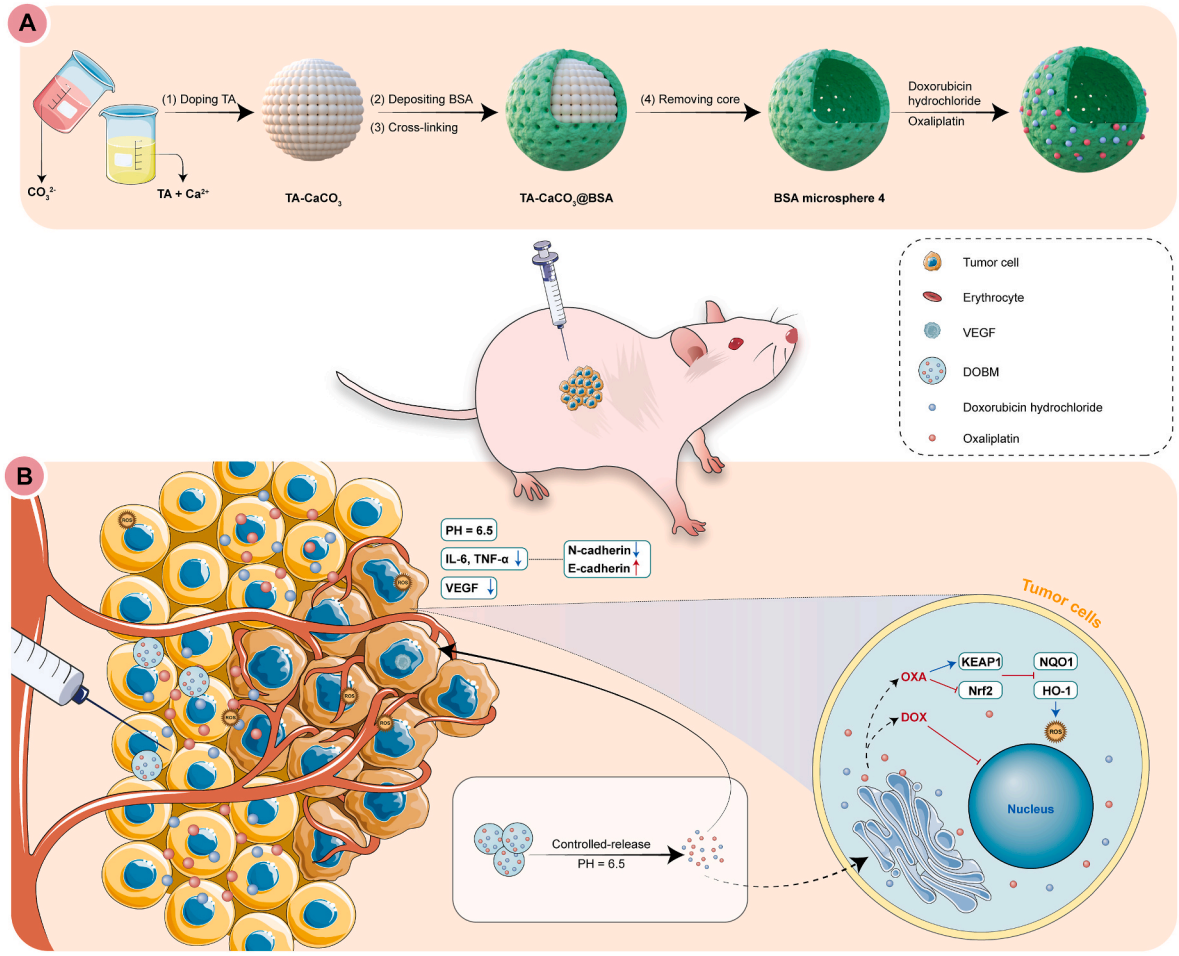

Scheme 1. Adriamycin/Oxaliplatin Dual-Carrier BSA Microspheres (DOBM) Synergistically Enhance Local Injection Treatment of HCC (generated at Biorender.com). (A) The DOBM establishment route. (B) DOBM were utilized in the mouse xenograft tumor model.

these patients after curative treatment is 60–70 % [4–6]. Systemic chemotherapy is the main palliative treatment for advanced HCC patients. Nevertheless, the systemically administered chemotherapy can cause severe side effects, particularly cardiac, hepatic, renal, and bone marrow suppression, due to the non-selective biodistribution of the chemotherapeutic agents in healthy tissues and organs. In addition, the relatively low bioaccessibility of these chemotherapeutic agents in the target tumor tissues, which can be rapidly cleared from the circulation, can result in low bioavailability, therefore severely compromising the therapeutic efficacy and resulting in an increased incidence of drug resistance [7–9]. Recently, local treatment of tumors has received extensive attention and has been widely investigated to maximize the efficiency of drug delivery [10–12]. Anti-cancer medications are injected locally into and around the tumor. They exhibit promising therapeutic advantages over systemic intravenous administration because of the highly selective accumulation and active cellular uptake of chemotherapeutic agents in the tumor. This not only reduces the required drug dose and improves the efficacy, but also avoids the toxicity of chemotherapeutic agents to normal cells throughout the body and minimizes the risk of off-target toxicity [8,12]. Therefore, it is expected that this highly concentrated delivery can enhance the safety and effectiveness of chemotherapy in cancer.

To address these issues, a wide range of drug carriers, including fibers, hydrogels, and liposomes, have been thoroughly synthesized for tumor therapy during the last decade [13–17].

Regardless of the advantageous methods and benefits of these drug carriers, there still exist several shortcomings. For example, the bioavailability of a medication can be impacted by the simple drug packaging, which can result in premature or quick drug release, short retention of therapeutic agent, and poor absorption of anticancer treatment by drug-resistant malignancies. Further research and development efforts are required to guarantee the ability of the carriers to provide many medications immediately. The synthetic polymers that are frequently used to create such carriers usually call for complex synthetic routes or extra chemicals, causing the difficult preparation procedures that are time-consuming and may trigger unintentional toxicities. However, biogenerated materials are simple to use in biomedical applications and reveal a good biocompatibility [18–24].

Therefore, it is essential to develop new drug delivery systems that use natural biopolymers to effectively load and release drugs for the local treatment and clinical applications in HCC.

In this study, a hollow bovine serum albumin (BSA) microsphere with multiple functionalities, which could be loaded with both adriamycin hydrochloride (DOX) and oxaliplatin (OXA), was prepared for the local treatment of HCC. Its synthetic route is schematically presented in Scheme 1A. Proteins are abundant in nature, which lay a candidate foundation for creating microscopic objects due to their highly repeatable, monodisperse structures and the accurately localized functional groups. The use of protein assemblies, protein capsules and protein cages has attracted considerable interest and has been widely investigated in recent years [25–32]. Among them, BSA is a naturally sourced protein characterized by good biocompatibility and biodegradability. Notably, it avoids the immune system, is non-immunogenic and possesses a strong drug binding capacity [33–37]. Therefore, effective cross-linking of BSA into protein microspheres for preparing new drug packaging systems can overcome the problem of lower drug loading

efficiency and achieve dual-drug loading, which is promising for the sustained and controlled release of drugs locally to the tumor and avoids the systemic toxicity of chemotherapeutic agents to a large extent. In this study, DOX and OXA were used as the model drugs, which were loaded simultaneously into BSA microspheres at a fixed ratio. DOX is an anthracycline drug that is highly toxic mainly to the heart. Many methods have been investigated to lessen its toxicity [38]. The third-generation platinum chemical OXA can selectively inhibit DNA replication, repair, and transcription in cancer cells by inducing nuclear DNA cross-linking at the N7 position of guanine and adenine [39]. The clinical use of DOX in combination with OXA chemotherapy causes positive pathological changes and prolongs patient survival compared with DOX treatment alone [40,41].

In this study, the research group previously employed a simple, versatile, efficient, and economical method to fabricate BSA microspheres, including (i) doping tannic acid (TA) in $CaCO_3$; (ii) removing BSA from $CaCO_3$ particles by utilizing 4-(4,6-dimethoxy-1,3,triazin-2-yl)-4-methylmorpholinium chloride (DMT-MM) for cross-linking BSA deposited on the surface of $CaCO_3$ while eliminating the $CaCO_3$ core; and (iii) enhancing protein adsorption by TA involved in TA-$CaCO_3$ particles through various interaction patterns such as hydrophobic-hydrophobic interaction, electrostatic interaction, hydrogen bonding, and van der Waals force, finally resulting in a uniform protein coating. This method was not influenced by isoelectric point (IEP), molecular weight, wettability, the applied protein functional domains or amino acid sequence, making sampling highly reproducible and stable [42]. The TA retained in the template showed properties such as anti-inflammation [43,44]. The, DOX and OXA were adsorbed on the surface of BSA microspheres by shaking at a fixed ratio. Due to the above-mentioned properties, the developed BSA microspheres had a large specific surface area and a high local retention capacity, which were the monodisperse microspheres with high injectability, tight surface pores that reduced drug leakage, high drug loading of hydrophilic drugs, and the ability to lower local inflammation. Through in vitro experiments, it was found that the drug-loaded BSA microspheres were pH-responsive, with better drug release in an acidic environment (namely, better release in the tumor microenvironment). Moreover, it released the drug in a fast-first-slow-first manner, which was expected to be absorbed by tumor cells. Based on in vivo experimental results, the drug-loaded BSA microspheres could effectively inhibit tumor growth and recurrence by remodeling the local tumor microenvironment and reducing inflammation, therefore inhibiting epithelial-mesenchymal transition (EMT), increasing oxidative stress (ROS), and achieving synergistic anti-tumor effects. As a result, they enhanced the local therapeutic efficacy against HCC in a mouse xenograft tumor model (Scheme 1B). Additionally, the biocompatibility of dual-loaded BSA microspheres was also demonstrated. These results suggest that the current dual-loaded BSA microspheres may be potentially used in the local injection therapy for HCC.

2. Materials and methods

2.1. Materials

DOX and OXA were obtained from Sigma-Aldrich Trading Co., Ltd. Human liver cancer PLC/PRF/5 cells, metastatic human liver cancer HCC-LM3 cells, and LO2 cells were provided by Shanghai Cell Center (Chinese Academy of Sciences). Fetal bovine serum and trypsin-EDTA were offered by Sigma-AldrichTrading Co., Ltd. BSA was provided by Sigma-Aldrich. Anti-Ki 67 antibodies were provided by Abcam (UK). Fluorescein (TUNEL) and in situ cell death detection kit were obtained in Roche (Indianapolis, IN, USA). Calcein-AM was provided by Thermo Fisher Scientific (USA). Each reagent used in immunofluorescence and immunostaining was utilized following manufacturer's protocols. Every chemical, 4-(4, 6-dimethoxy-1, 3,5-triazin-2-yl)-4-methyl morpholinium chloride (DMT-MM), sodium carbonate, or calcium chloride, was provided by Aladdin (China). Dialysis bags (MWCO = 1000 Da) were provided by Shanghai Yuanye Bio-Technology Co., Ltd. Anti-human BCL2 (ab32124-40, Abcam), anti-human BAX (ab32503-40, Abcam), anti-human N-cadherin (66219-1-Ig-50μl, Proteintech Group), anti-human E-cadherin (20874-1-AP-50μl, ProteintechGroup), anti-humanKEAP1 (10503-2-AP-50μl, Proteintech Group), and anti-human HO-1 (26416T, CST) were also used.

2.2. Preparation of the dual-loaded microspheres

The Na_2CO_3 solution was poured into a mixture of $CaCl_2$ and TA under 40 s of stirring at room temperature. The formed pellets were aged and centrifuged for 5 min to collect the TA-$CaCO_3$ microsphere pellets, which were rinsed three times using H_2O before collection and vacuum-drying overnight under 50 °C. The 2 mg/ml BSA solution was prepared with pH 6.8 HEPES buffer as the solvent. TA-$CaCO_3$ microspheres were added into BSA solution, followed by 2 h of shaking. The TA-$CaCO_3$ particles coated with BSA were rinsed with 10 mL HEPES, and washed twice to remove the remaining BSA prior to resuspension within DMT-MM solution (5 mL). Then, the samples were shaken for another 2 h before being centrifuged for 5 min to collect particles. Subsequently, the particles were rinsed with the HEPES buffer solution (10 mL) three times. The particles were incubated in an EDTA solution to remove the $CaCO_3$ core from the microspheres. The microspheres were rinsed three times using deionized water and centrifuged to obtain BSA microspheres (BM), which were later resuspended in H_2O and set aside.

Specifically,1 mg DOX powder was added into H_2O (10 mL) to prepare a solution, which was then blended thoroughly to obtain the DOX solution. Similarly, 3 mg OXA powder was added into H_2O (10 mL) to prepare the illustration, which was later mixed sufficiently to obtain the OXA solution. Afterwards, 3 mg OXA powder was introduced into 1 mg DOX powder and the mixture was subsequently added into H_2O (10 mL) after thorough mixing to obtain the DOX/OXA co-mixture solution. Next, prior to being centrifuged for 5 min at 3000 rpm, 10 mg BM was introduced into each of those three solutions for being incubated for 2 h on an oscillator. The procedure produced DOX, OXA and DOX/OXA microspheres (namely DBM, OBM and DOBM, respectively).

2.3. Physicochemical characterizations of the dual-loaded microspheres

The energy-dispersive spectroscopy (EDS) equipment was employed to obtain SEM images and EDS spectra of the test samples for surface analysis, while the material morphology and elemental content were observed under the JSM-7401F microscope [45].

Then, samples were analyzed by Fourier-transform infrared spectroscopy (FT-IR) with the TNZ1-5700 spectrometer (Nicolet, USA) at a scanning rate of 500–4000 cm−1. The X-ray photoelectron spectrometer was also used to investigate the characteristics and chemical states of the particles within a measuring range of 1200-0 cm $^{-1}$.

2.4. Drug loading and release characteristics of the dual-loaded microspheres

2.4.1. Drug loading behavior of the dual-loaded microspheres

Firstly, 10 mg DOX was transferred into a 10-mL volumetric flask. Then, deionized water was added to adjust the DOX concentration at 1 mg/mL. Secondly, aliquots of 0.0007812, 0.0015625, 0.003125, 0.00625, 0.0125, 0.025, 0.05, 0.1 and 0.2 mL solution were taken. Then, the aliquots were diluted sequentially in 10 mL volumetric flasks to obtain the 0.015625, 0.15625, 0.3125, 0.625, 1.25, 2.5, 5, 10, and 20 μg/mL solutions, respectively. Later, the absorbance value of every solution was determined with the UV spectrophotometer, and the standard curve was plotted [46]. After thoroughly vortexing test samples, the centrifugation was performed for 5 min at 2500 rpm to collect supernatants (200 μL) to measure absorbance using the UV spectrophotometer. Elemental contents in the acid-treated elemental ion solution were

directly detected by ICP-MSto to analyze the DOX and OXA levels in the supernatants (W1). The encapsulation efficiency (ER) was determined as follows.

$$ER\ (\%) = [(W - W1) / W] \times 100\%$$

where W represents the original drug loading level (mg).

2.4.2. Drug release characteristics of the dual-loaded microspheres

After the removal of supernatants, the drug-loaded microspheres were placed in the new 50 mL centrifuge tube for drug release. The release medium was phosphate buffer at the pH values of 6.5 and 7.4. The thermostatic shaker temperature was 37 °C and the shaker speed was 100 rpm. Sample collection was performed at 1, 2, 3, 4, 5, 6, 7, 8, 9, 10, 11, 12 h, 1, 2, 3, and 4 days, respectively. Immediately following every sample collection, blank release medium (phosphate buffer) at the same amount was added. Next, the sample absorbance values in DBM and DOBM groups were measured by the UV–visual photometer. Meanwhile, the elemental contents in the acid-treated elemental ion solution were directly detected by ICP-MS for each sample in OBM and DOBM groups, followed by the calculation of the cumulative drug release percentage in every group.

2.5. Biocompatibility studies in vitro

The biocompatibility of BM was determined by PLC/PRF/5, HCC-LM3, and LO2 cell proliferation assays.

PLC/PRF/5, HCC-LM3, and LO2 cells (2 × 10ˆ5 cells/mL) were inoculated in the 6-well plates.

Then, cells were classified into control and BSA microsphere groups, cultured for 24 h, and observed by calcein-AM staining.

Additionally, PLC/PRF/5, HCC-LM3, and LO2 cells were inoculated in 96-well plates added with 10 % FBS-containing DMEM at 8 × 10ˆ3 cells mL-1 under 5 % CO_2 and 37 °C conditions. The medium was eliminated following complete cell adherence. After washing once by PBS, cells were co-cultured with 10 % DMEM with the BSA microsphere suspension at varying concentrations (0, 25, 50, 100, 200 μg/ml) for 24 h, followed by incubation for 24 h with 10 % DMEM. Every well was introduced with CCNP (10 μL), and after being incubated for 2 h, cell viability was determined using a microplate reader at 450 nm.

2.6. Cell uptake efficiency

After 12 h of inoculation of PLC/PRF/5 and HCC-LM3 cells (2 × 10ˆ5/wells) in the confocal dishes, DOX and DBM (containing 1 μg/mL DOX) added in DMEM were introduced to incubate cells for another 6 and 12 h, respectively. The cell cytoskeletal structure was subjected to Actin-Tracker green and DAPI staining and then observed under the confocal laser scanning microscope (A1 Nikon Japan). PLC/PRF/5 and HCC-LM3 cells (2 × 10ˆ5/wells) were seeded into 6-well plates. After the cells completely adhered to the wall, BM (100 μg/mL) were added at 1, 2, 3, 4, 5, 6, 12 and 24 h, respectively. The medium was discarded after co-incubation. Then, cells were washed with the pre-warmed PBS once, and then with EDTA-free. Subsequently, cells were collected into the 15 mL centrifuge tubes with EDTA-free trypsin, followed by being centrifuged for 5 min at 1000 rpm and washing once by pre-warmed PBS. After the adjustment of cell density to (2–4) × 10ˆ6/mL, cells were resuspended in the EP tube. Following the removal of the supernatant, cells were resuspended by the addition of 300 μL DMEM and analyzed using flow cytometry.

2.7. Inhibition of the dual-loaded microspheres on HCC-LM3 and PLC/PRF/5 cells

To assess the in vitro cytotoxic effects of the dual drug-loaded microspheres, HCC-LM3 and PLC/PRF/5 human HCC cells were used as seed cells. This study was divided into five groups, including (1) DMEM (as negative control), (2) OBM, (3) DBM, (4) DOG ((free DOX + OXA as a positive control), and (5) DOBM groups.

2.7.1. MTT assay

The cells were digested, then inoculated into 96-well plates at 100 μL/well, and incubated at 37 °C with 5 % CO_2. When cells were fully adhered, the suspensions of DOX, OXA, DOG, as well as OBM, DBM, and DOBM containing DMEM (10 % FBS) at varying concentrations were added to incubate the cells for another 24 h. Then, MTT reagent (10 μL) was introduced into every well for MTT assay following the specific instructions.

2.7.2. Live/dead cell staining

The cells were digested, inoculated into 6-well plates, and incubated in the 5 % CO_2 incubator at 37 °C. Following complete adhesion, cells were rinsed once by PBS and subjected to respective treatments in the culture supernatants. After being co-cultured for 24 h, 4 mM calcein-AM (5 μL) was diluted with 10 mL DMEM, and each group was introduced with 500 μL cell staining solution. Next, the plates were incubated for 30 min at 37 °C in dark. Finally, the inverted fluorescence microscope was used to observe the cells.

2.7.3. Cell cloning experiment

The digested cells were inoculated into 6-well plates and incubated under 37 °C with 5 % CO_2. Following complete cell adherence, PBS was added to wash cells once, followed by the addition of different treatments into culture supernatants. After being co-cultured for 2 weeks, 4 % paraformaldehyde was added for 15 min cell fixation, followed by overnight staining with 1 % crystal violet, washing three times by PBS, and visualization.

2.7.4. Flow cytometry of cell apoptosis

Cells were digested and subsequently inoculated into 6-well plates under 37 °C with 5 % CO_2. Following complete cell adherence, diverse cell treatments were performed, followed by being incubated for 24 h. Then, cells were harvested into the 15 mL centrifuge tubes with EDTA-free trypsin, centrifuged for 5 min at 1000 rpm and washed by PBS twice. Later, cells were collected into the 15 mL centrifuge tubes with EDTA-free trypsin for being centrifugated for 5 min at 1000 rpm and washed by PBS twice. After the adjustment of cell density to (2–4) × 10ˆ6/mL, cells were resuspended in the EP tube. By removing the supernatant, binding buffer (300 μL) was introduced. Then, 5 μL membrane-bound protein FITC and 10 μL PI (Beyotime Biotechnology) were added into every EP tube to resuspend and incubate cells for 5 min prior to flow cytometry.

2.7.5. Measurement of intracellular ROS levels

PLC/PRF/5 and HCC-LM3 cells (2 × 10ˆ5/ml) were inoculated prior to 24 h of treatment in different groups. After removing the medium, DCFH-DA (1 mL, 10 μM) was introduced to each well at 37 °C with cells being incubated for 30 min away from light. Thereafter, flow cytometry and fluorescence microscopy were performed for sample analysis.

2.8. In vivo experiments of the dual drug-carrying microspheres

2.8.1. Establishment of a Balb/c mouse model of PLC subcutaneous graft tumor

Totally 25 five-week-old female BALB/c mice were split into five groups randomly, including PBS-treated group, OBM-treated group, DBM-treated group, DOG-treated group, and DOBM-treated group. The upper-middle groin of each mouse was cleaned, prepped, and then subcutaneously injected with 2.5 × 10ˆ6 cell suspension. Tumor development was monitored every day, and when the tumor volume reached 100 mm^3, 100 mg sample was injected into the tumor of each mouse every four days for therapy. Tumor volume and body weight were

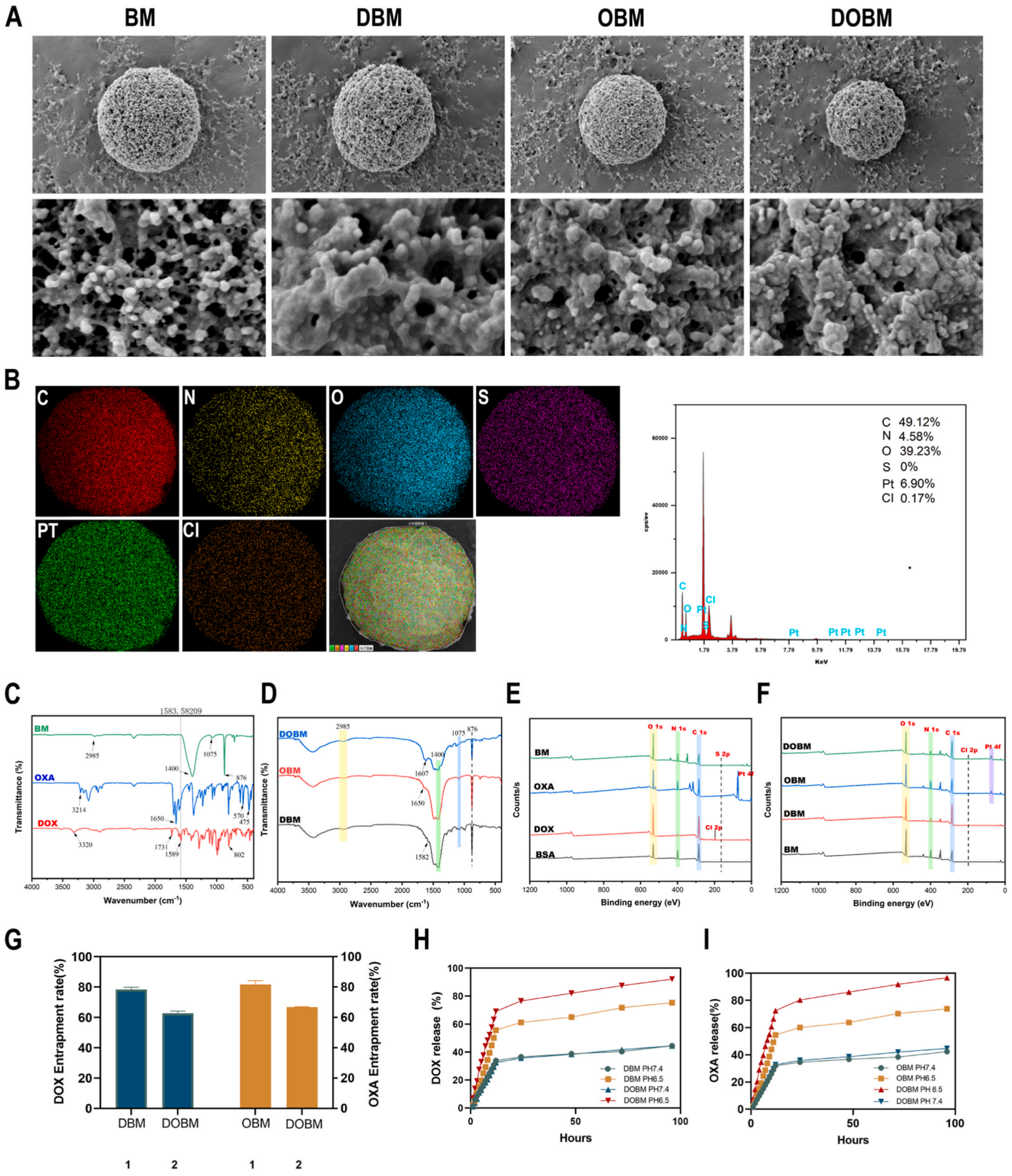

Fig. 1. Physicochemical characterizations. (A) Scanning electron microscopy (SEM) images under different magnifications, scale bars: 1 μm, and 100 nm. (B) Elemental composition, scale bar: 1 μm. (C) FT-IR spectra for DOX, OXA, and BM. (D) FT-IR spectra for DBM, OBM, DOBM. (E)XPS spectra for DOX, OXA, BSA, and BM. (F) XPS spectra for microspheres of different groups. (G) OBM, DBM, and DOBM encapsulation rates. (H) DBM and DOBM release profiles at varying PH values (pH 6.5, pH 7.4) (I) OBM and DOBM release profiles at varying PH values (pH 6.5, pH 7.4).

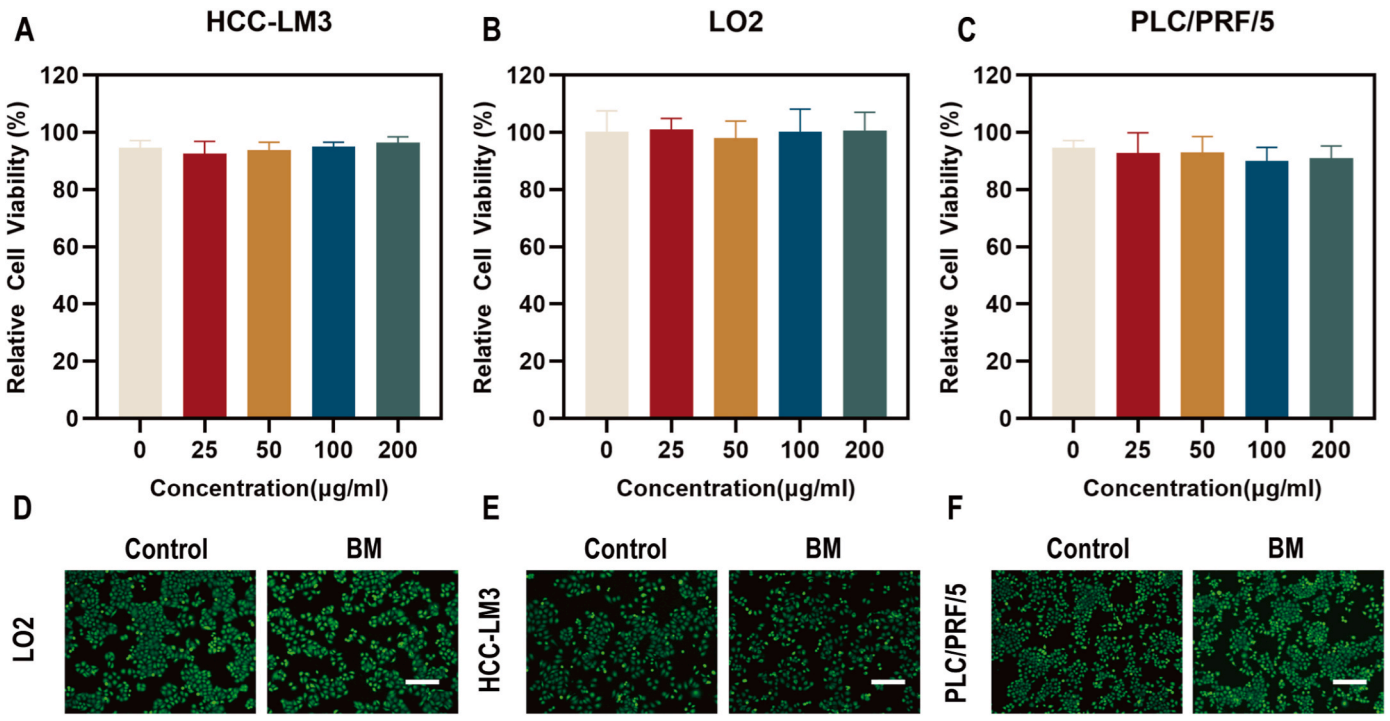

Fig. 2. BSA microsphere biocompatibility. (A–C) HCC-LM3 (A), LO2 (B), and PLC/PRF/5 (C) cell viability following 24 h of BM particle treatment at varying doses. (D–F) Fluorescence intensities of LO2 (D), HCC-LM3 cells (E) and PLC/PRF/5 cells (F) detected through Live cell staining after 24 h of co-incubation using 10 % FBS-containing DMEM and BM. Scale bar: 100 μm.

monitored every two days. Five groups were set, including (1) Control (PBS), (2) OBM, (3) DBM, (4) DOG, and (5) DOBM groups.

2.8.2. Histological staining and sampling

Following mouse euthanasia and photographing, tumors surgically resected were analyzed. After making a skin incision, the tumor was isolated from the neighboring muscle tissue layer by layer prior to photographing. Tumor tissues were stained with HE, IL-6, TNF-α, Ki-67, VEGF, tunnel, E-cadherin, and N-cadherin. Additionally, the heart, spleen, lung, kidney and liver samples were collected and stained with HE.

2.8.3. Biochemical analysis

Blood specimens of experimental rats were collected 2 weeks after local injection treatment. Then, cardiac, hepatic and renal function indexes including alanine aminotransferase (ALT), aspartate aminotransferase (AST), cardiac myosin profile (CK), creatine kinase isoenzyme (CK-MB), serum creatinine (Cr) and blood urea nitrogen (BUN) were examined.

2.9. Western blot assay

RIPA buffer (Beyotime Biotechnology, Shanghai, China) containing protease (APExBIO, K1007) and phosphatase inhibitor cocktail (C0002 and C0003, TargetMol) was added to lyse tumor tissues in xenograft or cells of different groups. The BCA Kit (Thermo Fisher Scientific) was employed to measure total protein content following the specific protocols. Protein separation was performed with SDS-PAGE, followed by transfer onto the polyvinylidene difluoride (PVDF) membrane. Next, membranes were blocked for 60 min using 5 % defatted milk, followed by overnight primary antibody incubation at 4 °C. After washing, membranes were subjected to 60 min of secondary antibody incubation under room temperature. Antibody binding was visualized with chemiluminescent HRP substrates (Millipore, Billerica, MA, USA).

2.10. Statistical analysis

The data were indicated as mean ± SD. Statistical analysis was performed with one-way ANOVA. *P < 0.05, **P < 0.01, ***P < 0.001, and ****P < 0.0001 represented statistical significance.

3. Results and discussion

3.1. Physiochemical characterizations of the drug-carrying microspheres

The SEM findings (Fig. 1A) indicated that the BM was spherical, with wide and irregularly distributed pores on the rough surface. There were drug crystals on the surfaces of DBM, OBM, and DOBM, and their shapes were comparable to those of BM. Particle size analysis (Fig. S1B) suggested that the BM particles were concentrated at approximately 2000 nm. The diameters of DBM, OBM, and DOBM were increasing and primarily concentrated at around 2300 nm, with the diameter of DOBM representing the largest increase. This could be explained by the homogeneous drug adsorption on the surface of BM. In addition, the SEM images in Fig. 1A provided high magnification images showing the surface morphology of BM, OBM, DBM and DOBM after lyophilization. The surfaces of drug-loaded BSA microspheres (OBM, DBM, and DOBM) were covered by drug crystals to varying degrees, and some pores on the surface of BM disappeared. DOBM had the most drug crystals adsorbed on the surface and the least surface pores, demonstrating that the surface modification of BSA microspheres by drug crystals (DOX, OXA) was successful (Fig. 1A).

EDS elemental mapping was employed to investigate DOBM. There were different elements (C, N, O, S, Pt, and Cl) labeled onto the DOBM sample surface with different colors, as shown in Fig. 1B. The main components of BSA were C, N, O, and S, while those of BM were also C, N, O, and S, and those of DOX were C, N, O, and Cl, while those of OXA were C, N, O, and Pt. The EDS data demonstrated that DOBM was effectively loaded with both DOX and OXA since C, N, O, S, Pt, and Cl elements were uniformly distributed on the surface of the DOBM

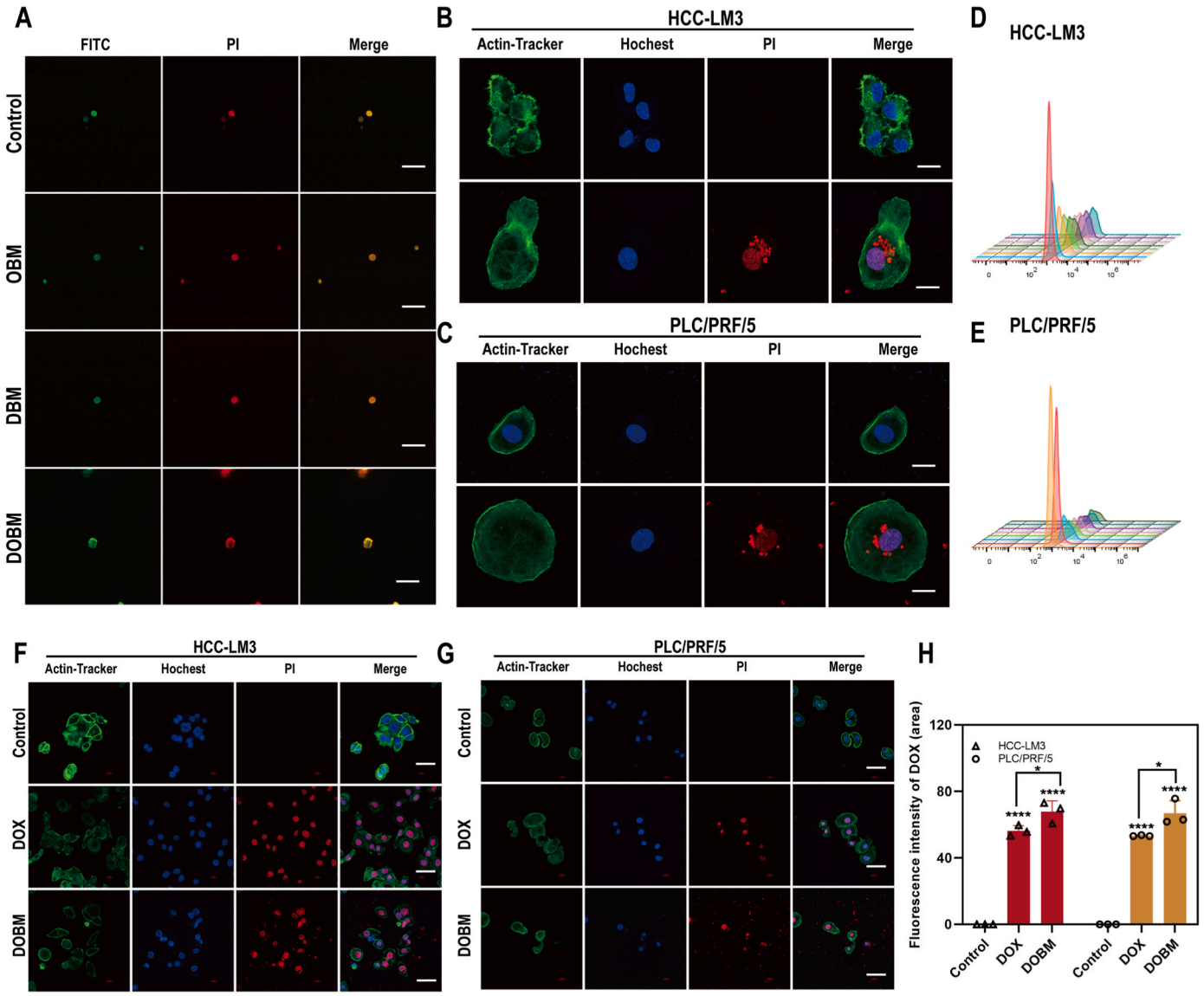

Fig. 3. Laser confocal scanning microscopy for observing the uptake of DOBM and DOX by HCC-LM3 and PLC/PRF/5 cells. (A) Red and green fluorescence emissions from BM, OBM, DBM, and DOBM groups under the excitation light were examined using a confocal laser scanning microscope. (B, C) DOBM cellular uptake into HCC-LM3 and PLC/PRF/5 cells measured through a confocal laser scanning microscope. Fluorescence staining images representing HCC-LM3 (B) and PLC/PRF/5 (C) cells after co-incubation with DMEM and DOBM for 12 h. Scale bars: 20 μm. (D, E) Flow cytometry conducted using FITC-Annexin V/PI for the detection of DOBM cytophagocytosis by HCC-LM3 (D)and PLC/PRF/5(E) cells after 0, 1, 2, 3, 4, 5, 6, 12 h of DOBM treatment. (F, G) The fluorescence staining images showing HCC-LM3 (F) and PLC/PRF/5 (G) cells co-incubated using DOX, DMEM, and DOBM for 6 h. Nucleus (blue), Cytoskeleton (green), DOBM (red), DOX (red). Scale bar: 20 μm (H) Quantitation of DMEM, DOX, and DOBM intensities in HCC-LM3 and PLC/PRF/5 cells (*. a significant difference compared with the DOX group).

microspheres.

X-ray photoelectron spectroscopy (XPS) (Fig. 1E and F) and FT-IR (Fig. 1C and D) were used to verify the loading of medicines on the BM surface. Fig. 1C presents the IR spectra of the raw materials DOX, OXA, and BM. A broad peak measured at 3320 cm^{-1} for DOX was caused by the telescopic vibration peak of the O-H bond in the material; besides, a potent peak at 1731 cm^{-1} was the telescopic vibration peak of C=O, representing the benzoquinone portion, and ester group of DOX; while the peak at 1589 cm^{-1} corresponded to the bending vibration peak of N-H, that at 802 cm^{-1} was associated with C-H vibration outside the benzene ring, and that at 802 cm^{-1} was related to C-H vibration outside the benzene ring. For OXA, a peak detected at 3214 cm^{-1} was resulted from the N-H stretching vibration peak; that detected at 1650 cm-1 was the C=O stretching vibration peak; and, most importantly, that appeared at 475 cm-1 was the Pt-O vibration peak, while that occurred at 570 cm^{-1} was correlated with Pt-N vibration, which was a characteristic peak of OXA. From the IR spectra for BM, the peak detected at 2985 cm^{-1} was associated with C-H stretching vibration in the aliphatic chain; that at 1400 cm^{-1} was related to C=O bending vibration of carboxylic acid; that measured at 1075 cm^{-1} was associated with C-N bond stretching vibration of amino acid and polypeptide; in addition, a sharp peak appearing at 876 cm-1 was associated with C-H bending vibration peak in the benzene ring. It was observed in Fig. 1D that DBM, OBM, and DOBM exhibited the characteristic infrared peaks belonging to BM at 2985 cm^{-1}, 1400 cm^{-1}, 1075 cm^{-1}, and 876 cm^{-1} in the infrared spectra of microspheres. This suggested that the blank BM were used as carriers to carry the drug. However, the infrared spectrogram of DBM microspheres exhibited a weak N-H bending vibrational peak at 1582 cm^{-1}, indicating that DOX was successfully filled into the blank BM. In the IR spectrogram of OBM microspheres, the C=O stretching vibrational peak was observed at around 1650 cm^{-1}, indicating the successful incorporation of OXA. In DOBM, the C=O

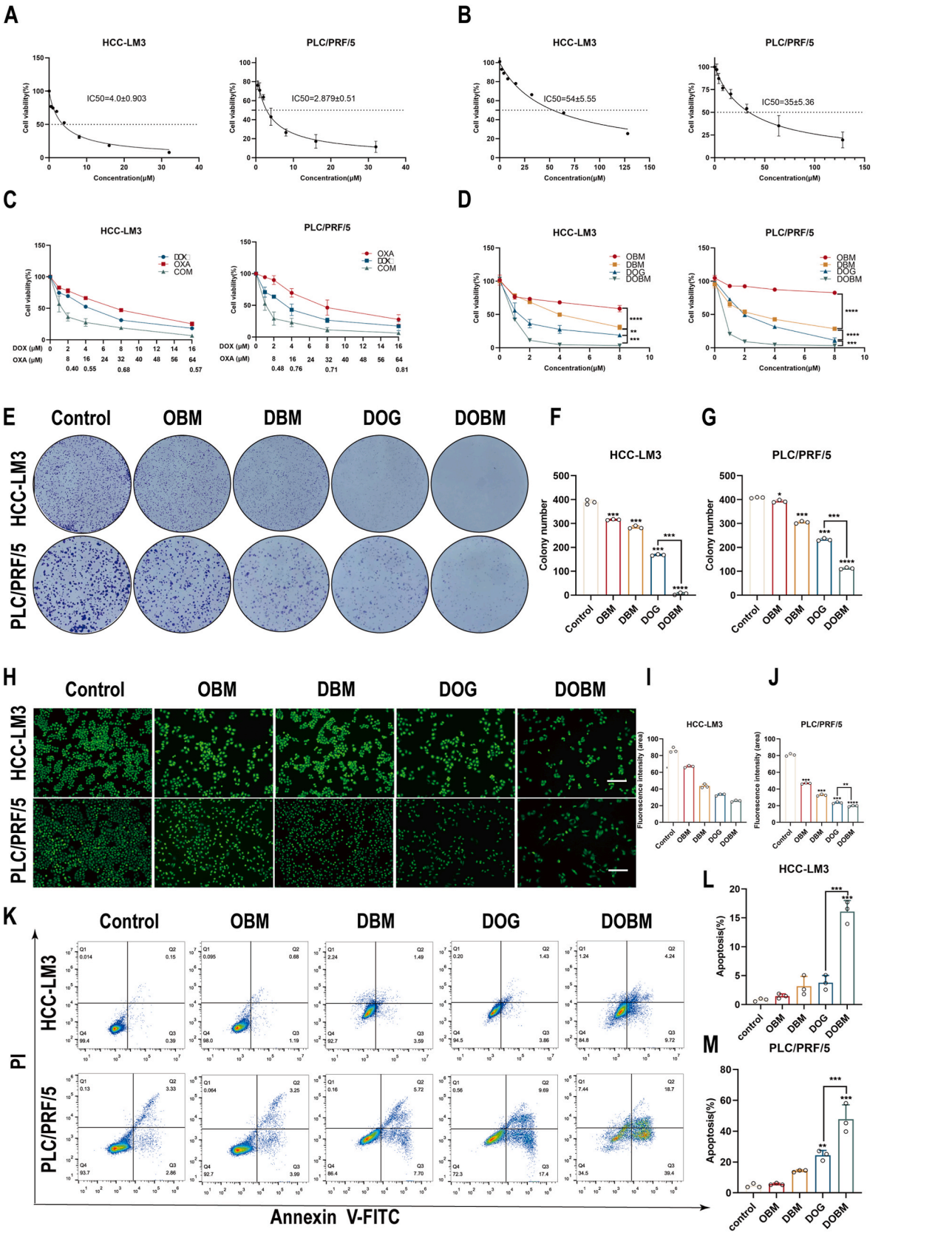

(caption on next page)

Fig. 4. Cytotoxicity and in vitro inhibition of DOBM. IC50 values of adriamycin hydrochloride (DOX) (A) and Oxaliplatin (OXA) (B) on HCC-LM3 and PLC/PRF/5 cells were measured through MTT assay. (C) Determination of the effects of DOX, OXA, and combination treatment on cell viability of HCC-LM3 and PLC/PRF/5 cells. CI values were calculated at each dose with the CompuSyn software. (D) Inhibitory effects of varying concentrations of OBM, DBM, DOG, and DOBM on HCC-LM3 and PLC/PRF/5 cells detected through MTT assay. (E–G) Colony formation assay performed to detect the impacts of DMEM, OBM, DBM, DOG and DOBM (for DOX (HCC-LM3: 2 μM, PLC/PRF/5: 2 μM); for OXA (HCC-LM3: 8 μM, PLC/PRF/5: 8 μM), and combinations (HCC-LM3: 2 μM + 8 μM, PLC/PRF/5: 2 μM + 8 μM)) on HCC-LM3 and PLC/PRF/5 cell proliferation. (H–J) Microscopic observation of DMEM, OBM, DBM, DOG and DOBM (DOX (HCC-LM3: 2 μM, PLC/PRF/5: 2 μM), OXA (HCC-LM3: 8 μM, PLC/PRF/5: 8 μM), and combinations (HCC-LM3: 2 μM + 8 μM, PLC/PRF/5: 2 μM + 8 μM)) in the co-culture with HCC-LM3 and PLC/PRF/5 for 24 h and corresponding quantitative results. PRF/5 cells (2 μM + 8 μM) were co-cultured with HCC-LM3 and PLC/PRF/5 for 24 h. Live cell staining and quantification were completed. Scale bar: 100 μm. (K–M) DMEM, OBM, DBM, DOG, and DOBM (DOX (HCC-LM3: 2 μM, PLC/PRF/5: 2 μM), OXA (HCC-LM3: 8 μM, PLC/PRF/5: 8 μM), and combinations (HCC-LM3: 2 μM + 8 μM, PLC/PRF/5: 2 μM + 8 μM)) were applied to HCC-LM3 and PLC/PRF/5 cells for 24 h. Apoptosis was performed using flow cytometry. Results are indicated by mean ± SD (n = 3). ((*P < 0.05, **P < 0.01, ***P < 0.001, ****P < 0.0001).

vibrational peak belonging to DOX was also found, but the Pt-O and Pt-N bonds belonging to OXA could not be found in this IR spectrogram. Probably, it was because that the Pt content in the sample was too low to form a clear absorption peak. The full XPS spectra of BSA, DOX, OXA, and BM are shown in Fig. 1E.

BSA and BM exhibited only elemental peaks of C, O, N, and S, suggesting that there existed no change after constructing the TA-$CaCO_3$ template by adsorbing, cross-linking and denuclearizing BSA to synthesize the blank BM. The elemental peaks of Cl 2p at 199 eV for DOX and Pt 4f at 73 eV for OXA stood for their respective characteristic elemental peaks. As displayed in Fig. 1F, the Cl 2p peak appeared in the material after BM was loaded with DOX, and the appearance of Pt could be seen after BM was loaded with OXA. Finally, the elemental peaks of Cl and Pt were seen in the XPS full spectrum after BM was loaded with DOX and OXA simultaneously, indicating that the two drugs were simultaneously loaded into the microspheres, and that the preparation of the dual-loaded microspheres was successful.

Drug loading and release are the crucial metrics for assessing how well drug-loaded microspheres work. When BM was loaded with a single drug, the encapsulation rates of DOX and OXA were 78.41 ± 1.43 % and 81.67 ± 2.52 %, respectively, based on the findings of encapsulation efficiency (Fig. 1G). Concurrent loading of BM with DOX and OXA caused a modest reduction in the encapsulation rates, which were 62.74 ± 1.56 % and 66.68 ± 0.33 %, respectively. Our findings demonstrated that co-loading the two medications exerted little impact on the drug loading efficiency; nevertheless, the encapsulation rate remained over 50 %, which ensured the high drug loading efficiency.

The degradation behavior of BM, OBM, DBM, and DOBM in phosphate buffer (pH 6.5) was examined. SEM results demonstrated that the BSA microspheres (BM, OBM, DBM, and DOBM) developed in this study remained approximately spherical after incubation under acidic conditions for 3, 7, 15, and 30 days, and that obvious pores could be observed. The drug-loading process exerted no influence on the degradation rate of the BSA microspheres, indicating that the drug-loaded BSA microspheres were well stabilized under slightly acidic conditions, and that the degradation rate could satisfy the requirements for topical injection therapy and maintain the requirements for long-term drug slow release (Fig. S1 A).

In vitro, drug release behaviors of OBM, DBM, and DOBM were investigated at varying pH values (pH 6.5, pH 7.4), with PBS as a release medium. As shown in Fig. 1I and J, on day 4, the cumulative DOX release rates were 75.379 ± 0.01 % and 44.56 ± 1.53 % for DBM and 92.21 ± 0.01 % and 44.56 ± 0.01 % for DOBM, respectively, at pH 6.5 and pH 7.4. Similarly, for OXA, the cumulative release rates of OBM were 73.89 ± 0.01 % and 42.37 ± 1.23 % at pH 6.5 and pH 7.4, respectively, while those of DOBM were 96.67 ± 0.01 % and 44.74 ± 1.45 % at pH 6.5 and pH 7.4, respectively. Therefore, DBM, OBM, and DOBM all remained stable in vitro drug release in different pH environments and were able to prolong and control drug release to satisfy the pharmacological requirements of clinical therapy. The release of DOX and OXA was faster and the final cumulative release rate was higher in slightly acidic tumor microenvironments. This indicated that the successive releases of DOX and OXA from the DOBM were responsive to pH. The fast-then-slow, pH-sensitive, and persistent DOX and OXA release could result in a rapid killing of tumors, followed by the maintenance of the effective drug concentration and the sustained antitumor effect in tumors.

3.2. Biocompatibility evaluation

To assess the in vitro cytotoxicity induced by BM, varying doses (0, 25, 50, 100, 200 μg/ml) of BM were added to incubate LO2, PLC/PRF/5, and HCC-LM3 cells for 24 h. No significant statistical differences were observed, and a minor variation in cell viability was observed at every dose (Fig. 2A–C). Cytotoxicities induced by BM to LO2, PLC/PRF/5, and HCC-LM3 cells were analyzed by live-cell staining. Therefore, the BM group exhibited a close fluorescence intensity to the control group (with no BM) (Fig. 2D, E, and F). Meanwhile, mouse erythrocytes (2 % v/v) were treated with different masses of BM for hemolysis test. Then, the OD value of the supernatant was determined. It was found that the supernatants of different masses of BM were colorless and close to the negative control. In addition, erythrocyte fragmentation resulted in a scarlet color in the supernatant of the positive control. Additionally, the HR of BM treatment was lower than 5 % of the maximum limit, indicating that BM had a high blood compatibility (Fig. S2A). These results suggest that BM exhibit a high biocompatibility and are not harmful to cells.

3.3. Cellular uptake

The emission of red and green fluorescence from OBM, DBM, and DOBM drug-loaded microspheres, as well as blank BM under the excitation light was examined using a confocal laser scanning microscope. Fluorescence intensity of the blank BM revealed no significant change during the drug-loading process (Fig. 3A). Confocal laser scanning microscopy was performed to investigate the DOBM adsorption into HCC-LM3 and PLC/PRF/5 cells (Fig. 3B and C). The uptake of DOBM by HCC-LM3 (Fig. 3D) and PLC/PRF (Fig. 3E) cells was measured using flow cytometry. The cytophagy of DOBM by cancer cells slightly increased as time went by, peaking at 12 h. Confocal laser scanning microscopy was performed to analyze the adsorption of DOX- and DOBM-released DOX into HCC-LM3 and PLC/PRF/5 cells (Fig. 3F and G). The fluorescence intensity of DOBM was slightly stronger than that of DOX group (Fig. 3H). These findings suggest that DOBM have strong cellular phagocytosis, DOX encapsulated by DOBM show stronger endocytosis, and BM exert no influence on the phagocytosis of DOX, which can further enhance the cytotoxic effect on tumor cells.

3.4. Cytotoxicity and in vitro inhibition of OBM, DBM, DOG and DOBM

To create the drug-loaded microspheres, cytotoxicity is of great importance. MTT assay, colony formation assay, Annexin V/PI flow cytometry and live cell staining kit were used to assess the killing effects of OBM, DBM, DOG, and DOBM against HCC-LM3 and PLC/PRF/5 cells. To assess the synergistic inhibitory effects of DOX and OXA on HCC cell survival, DOX and OXA alone were applied to treat HCC-LM3, and PLC/PRF/5 cells. After 24 h, MTT assay was performed to measure cell survival. Therefore, DOX and OXA monotherapies suppressed HCC cell viability dose-dependently. IC50 levels of DOX in HCC-LM3 and PLC/

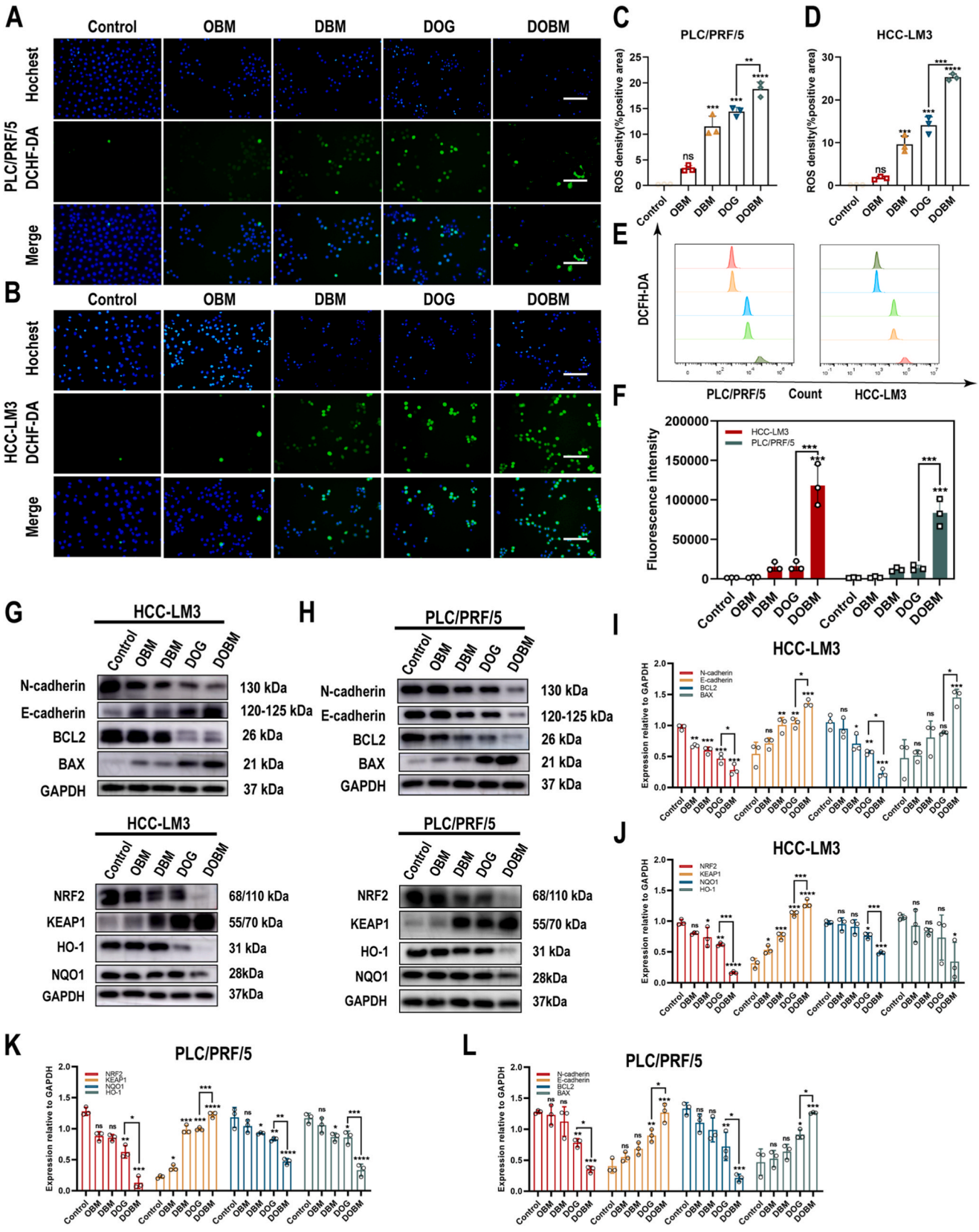

Fig. 5. Mechanisms of reducing ROS accumulation. (A, B) ROS concentrations in PLC/PRF/5(A) and HCC-LM3(B) cells of DMEM, DOG, DOBM, OBM, and DBM groups; Scale bar: 100 μm. (C, D) Average ROS fluorescence intensity in (A, B). (E) Detection of ROS levels in different groups using flow cytometry. (F)Average ROS fluorescence intensity in (E). (G–L) BAX, BCL2, N-calmodulin, E-calmodulin, NRF2, KEAP1, NQO1, and HO-1 levels in HCC-LM3 and OLC/PRF/5 cells measured through Western blot assay. Results are indicated by mean ± SD (n = 3). (*P < 0.05, **P < 0.01, ***P < 0.001, ****P < 0.0001).

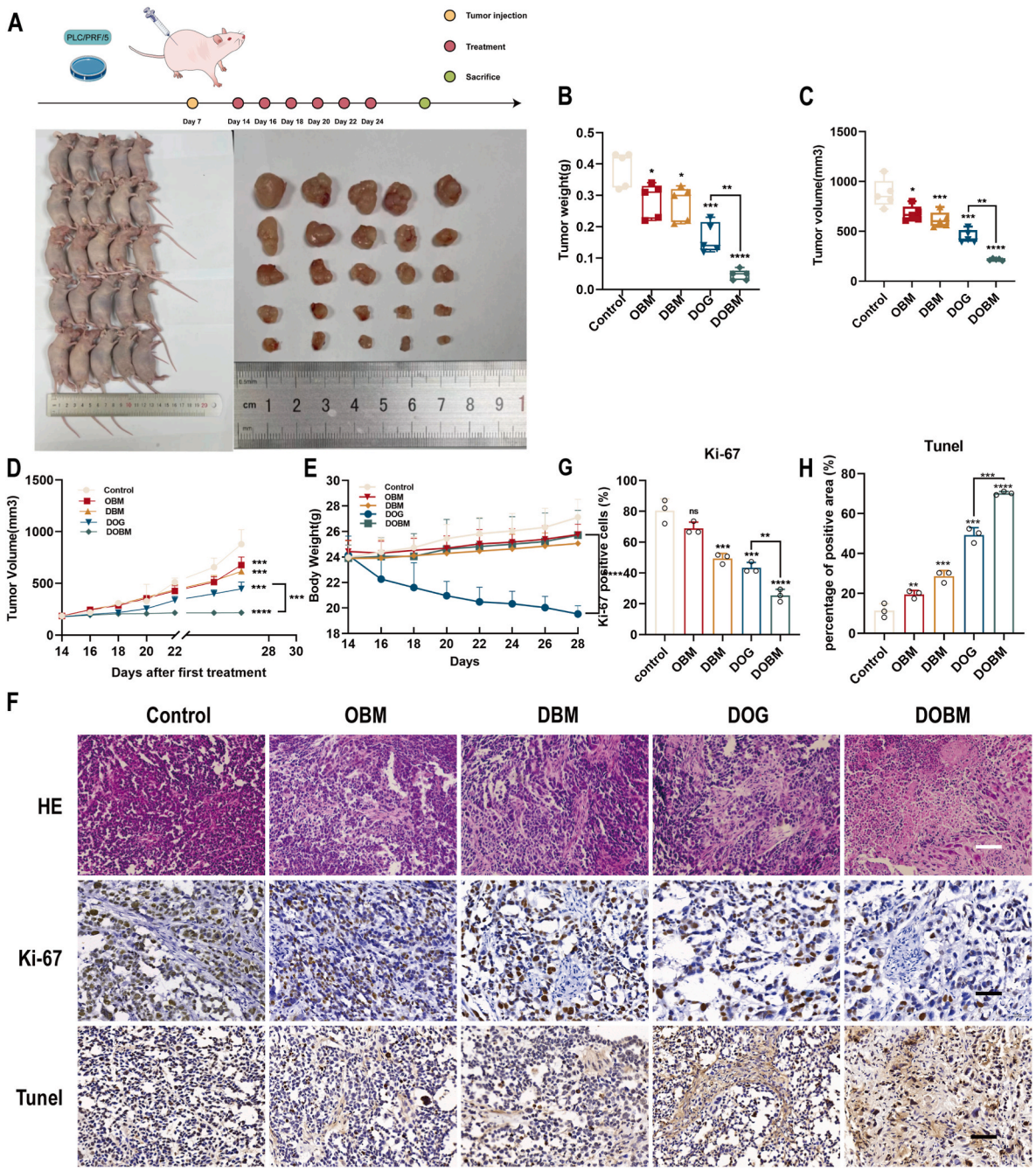

Fig. 6. Inhibition of DOBM against the subcutaneous PLC/PRF/5 tumor xenograft of Balb/c-nu mice. (A) Schematic diagram of the construction and treatment of the mouse model of PLC/PRF/5 subcutaneous tumor xenograft. Images of tumors in PLC/PRF/5 xenografts treated with various agents. Final tumor weight (B) and volume (C) of xenografts after various therapies are shown in (B and C). (D) Growth curves for tumors under various interventions. (E) Tracking the changes in mouse weight in response to various treatments. (F) Images representing hematoxylin-eosin (HE), Ki-67, and TUNEL immunohistochemical (IHC) staining for tumor tissues collected in different groups (all tissues: × 200). The change in the tumor's basic state was monitored by HE staining. The brown areas in Ki-67 and TUNEL staining indicated Ki-67-positive and TUNEL-positive cells, respectively. (G) The Ki-67-positive cell index of every group was calculated. (H) The TUNEL-positive cell index of every group was identified by the apoptotic cell-to-total cell ratio in every field. Results are indicated by mean ± SD (n = 3). Scale bar; 50 μm. (*P < 0.05, **P < 0.01, ***P < 0.001, ****P < 0.0001).

PRF/5 cells were 4.0 ± 0.90 μM and 2.87 ± 0.51 μM, respectively (Fig. 4A), and those of OXA were 54 ± 5.50 μM and 35 ± 5.36 μM, respectively (Fig. 4B). To evaluate the synergistic effect of DOX and OXA, Calcusyn software (Biosoft, Cambridge, UK) and Chou-Talalay method were used. The combination index (CI) which is less than 1 suggests the synergistic effect of drug combinations. The CI values for the combination of DOX and OXA were as low as 0.40 and 0.48 in HCC-LM3 and PLC/PRF/5 cells (Fig. 4C), indicating that the combination of DOX and OXA had a strong synergistic activity at this concentration. To further explore the anti-tumor proliferative effects of dual-loaded microspheres, the time-dependent effects of DBM, OBM, DOG, and DOBM on the above two cells lines were examined using MTT assay. The DOBM dual-loaded microspheres showed a stronger potency of inhibiting HCC cell proliferation than the single-loaded microspheres and the direct two-drug combination groups (Fig. 4D). Clone formation assays indicated that the DOBM group had the least colonies following 2 weeks of

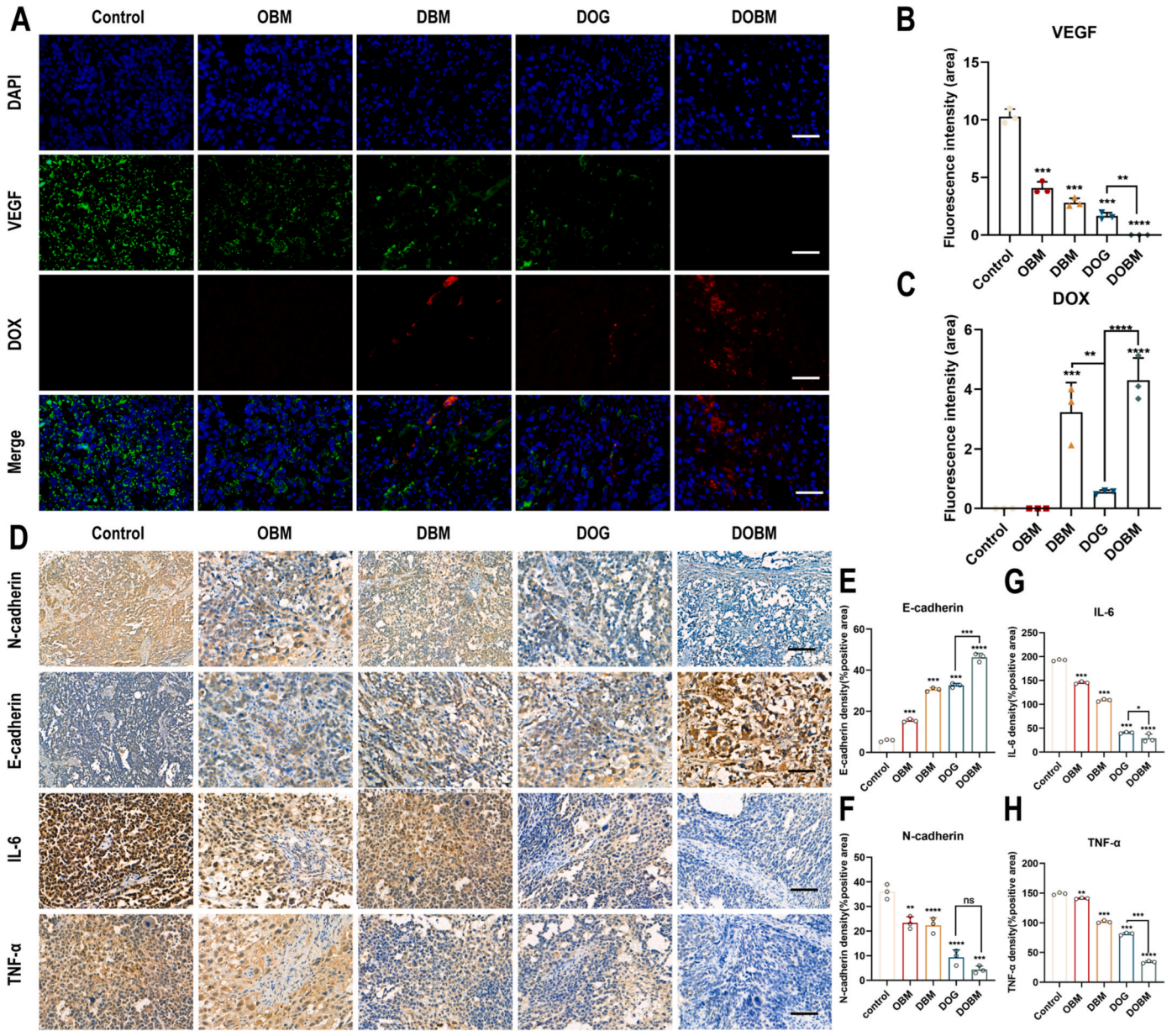

Fig. 7. Mechanisms of the combined antitumor and anti-metastatic effects in vivo. (A) Images showing VEGF immunofluorescence (IF) staining and DOX fluorescence imaging for tumor tissues collected in different groups. Nuclei were stained with DAPI. Green and red fluorescence indicates VEGF and DOX levels in tumor tissues. (B) The fluorescence intensity of the VEGF-positive area in every group was determined. (C) The fluorescence intensity of the DOX-positive area in every group was identified by residual DOX level in the tissue. (D) Images showing IHC staining for E-cadherin, N-cadherin, IL-6, and TNF-α in tumor tissues collected from different groups. The E-cadherin-positive (E), N-cadherin-positive (F), IL-6-positive (G), and TNF-α-positive (H) area intensities of every group were determined. Results are indicated by mean ± SD (n = 3). Scale bar: 50 μm. Data are indicated by mean ± SD (n = 3). (*P < 0.05, **P < 0.01, ***P < 0.001, ****P < 0.0001). (Color interpretation of the figure can be found from the online version).

co-incubation compared with the OBM.DBM.DOG groups (Fig.E–G). In addition, viable cell staining analysis conformed to MTT and colony formation assays, significantly decreasing the viable cell percentage of DOBM group, with the statistically significant difference between DOBM and DOG groups (Fig. 4H–J). Live cell staining and quantification of DMEM, OBM, DBM, DOG, and DOBM groups were performed following 24 h of co-incubation in HCC-LM3 and PLC/PRF/5 cells. Scale bar: 100 μm. HCC-LM3 and PLC/PRF/5 cell apoptosis in each group following 24 h of treatment was measured by FITC-Annexin V/PI flow cytometry. As shown in Fig. 4K–M, the total apoptotic numbers of HCC-LM3 cells in each group were 0.82 ± 0.26 %, 1.46 ± 0.41 %, 3.17 ± 1.71 %, 3.79 ± 1.26 %, and 16.08 ± 1.92 %, respectively, and those of PLC/PRF/5 cells were 4.63 ± 1.34 %, 5.62 % ± 0.62 %, 14.17 ± 0.65 %, and 24.38 ± 3.14 %, respectively, after being co-cultivated with DMEM, OBM, DBM, DOG, and DOBM for 24 h. The findings demonstrate a substantial difference in the Ming's total apoptotic cell rate between the DOBM group and the DOG group. By examining the apoptotic data, DOBM were more effective on killing HCC cells than OBM, DBM, and DOG. This suggests that OXA and DOX may work in concert to combat tumors and that the drug-loaded microspheres may exert a greater anti-tumor impact.

3.5. Inhibition on reactive oxygen species accumulation

ROS are known to be essential for a number of biological functions [47,48], and disturbances in the redox equilibrium have the potential to permanently harm cells, which is a phenomenon that has been

Table 1
Main pharmacokinetic parameters of DOX (1 mg/kg) in mice treated with DOG and DOBM.group A, DOG group; group B, DOBM group; (n = 5, mean ± SD).

parameters	unit	A	B
$t_{1/2}$	h	2.79 ± 0.48	13.92 ± 3.20**
T_{max}	h	0.5	1.00
C_{max}	μg/mL	2.67 ± 0.57	2.29 ± 0.18
AUC_{0-t}	μg·h·mL^{-1}	6.70 ± 1.29	31.32 ± 3.74***
$AUC_{0-\infty}$	μg·h·mL^{-1}	6.96 ± 1.27	34.31 ± 4.68***
$MRT_{0-\infty}$	h	3.32 ± 0.61	19.20 ± 3.29***
Vd	L·kg^{-1}	0.60 ± 0.17	0.59 ± 0.12
CL	L·h^{-1}·kg^{-1}	0.15 ± 0.03	0.03 ± 0.004***

**p < 0.01, significant in comparison with group A; ***p < 0.001, significant in comparison with group A.

Table 2
Main pharmacokinetic parameters of OXA (3 mg/kg) in mice treated with DOG and DOBM.group A, DOG group; group B, DOBM group; (n = 5, mean ± SD).

parameters	unit	A	B
$t_{1/2}$	h	2.56 ± 0.47	12.01 ± 3.52**
T_{max}	h	1.00	2.00
C_{max}	μg/mL	3.86 ± 0.31	3.51 ± 0.29
AUC_{0-t}	μg·h·mL^{-1}	13.59 ± 1.54	51.30 ± 8.22***
$AUC_{0-\infty}$	μg·h·mL^{-1}	14.05 ± 1.63	54.60 ± 9.44***
$MRT_{0-\infty}$	h	3.75 ± 0.53	15.23 ± 3.48**
Vd	L·kg^{-1}	0.79 ± 0.15	0.96 ± 0.26
CL	L·h^{-1}·kg^{-1}	0.22 ± 0.03	0.06 ± 0.01***

**p < 0.01, significant in comparison with group A; ***p < 0.001, significant in comparison with group A.

connected to therapeutic resistance, metastasis, and cancer [49]. Relative to the control group, the DOBM group had significantly increased intracellular ROS levels in HCC-LM3 and PLC/PRF/5 cells, as observed from Fig. 5A–F. Western blot assay of ROS and apoptotic indicators also corroborated these results (Fig. 5G–L). In both cell lines, Bax, KEAP1, and E-cadherin levels significantly increased in DOBM group relative to OBM group, DBM group and DOG group, while NRF2, HO-1, NQO1, N-cadherin and Bcl-2 levels significantly decreased. Meanwhile, ROS production in DOBM group obviously increased by over 50 %, and the difference was of statistical significance relative to DOG group. The obtained results demonstrate that the DOBM group inhibits HCC cell growth and migration by increasing the cellular mitochondrial ROS expression.

3.6. Observation of histopathological changes in tumors

The subcutaneous PLC/PRF/5 xenograft tumors were created in nude mice in vivo. The animals were randomly assigned to five groups, and received treatments with PBS, OBM, DBM, DOG, and DOBM every four days. As expected, direct administration of DOX and OXA therapies revealed a modest reduction of tumor development. Compared with direct treatment, DOBM exerted a much stronger tumor-inhibitory effect, which caused a reduced tumor growth rate, volume, and weight (Fig. 6A–D). Importantly, we found significant differences in weight and significant signs of toxicity in the direct drug administration group compared with the other three drug-loaded microsphere groups, suggesting that the drug-loaded microsphere group well tolerated drug administration relative to direct chemotherapeutic drug treatment group (Fig. 6E). All mice were necropsied, and tumor tissues were collected to perform different pathological staining at 2 weeks post-local injection. Basic tumor status and necrosis were observed post-treatment through H&E staining. As presented in Fig. 6F, cell nuclei in control tumors were tightly arranged. By contrast, the tumors in DBM, OBM, DOG, and DOBM groups exhibited obvious signs of cell necrosis, with the area of necrosis in the DOBM group being much larger than those in the other treatment groups. Ki-67 is a key marker for tumor cell proliferation [50]. Our results demonstrated that the Ki-67-positive cell proportions in control, OBM, DBM, DOG and DOBM groups were 80.41 ± 7.64 %, 68.97 ± 4.04 %, 49.47 ± 3.22 %, 43.37 ± 3.46 %, and 25.38 ± 4.00 %, respectively. The Ki-67-positive cell proportion of DOBM group significantly decreased relative to those in the remaining three treatment groups, exhibiting the superior anticancer effect of DOBM on tumor cell proliferation (Fig. 6F and G). Meanwhile, the apoptotic cell index values of control, OBM, DBM, DOG, and DOBM groups were 11.33 ± 3.51 %, 19.59 ± 1.94 %, 28.65 ± 2.89 %, 49.33 ± 3.65 %, 70.21 ± 0.89 % and 85 ± 6.00 %, respectively, as measured through TUNEL staining. Therefore, DOBM-treated mice had the greatest apoptosis rate among different groups (Fig. 6F–H). Ki-67 staining led to similar results to TUNEL IHC staining, demonstrating the better antitumor effect of DOBM than OBM, DBM, and DOG. Therefore, DOX combined with OXA exerted the synergistic antitumor effect and DOX/OXA loaded into BM had a better antitumor effect than that of the drug alone.

3.7. The anti-tumor and anti-metastatic mechanisms

VEGF is a key angiogenic factor for tumor tissue, showing a close relationship with the anti-tumor efficacy of tumor cell growth. To further investigate and comprehend the possible mechanisms of DOBM with their anti-tumor and anti-metastatic actions, VEGF expression and the residual DOX level were investigated in tumor tissues. Fig. 7A displays the representative photos of VEGF IF-stained tumor tissues of different groups. The VEGF-positive region in DOBM group showed a considerably lower fluorescence intensity, as demonstrated by IF staining, relative to the control, OBM, DBM, and DOG groups, with the statically significant difference (Fig. 7B). Next, we evaluated the role of DOBM in inhibiting angiogenesis in vitro through the HUVECs tube formation assay. Compared with the DMEM, OBM, DBM, and DOG groups, the DOBM group showed fewer tubular structures (Fig. S3A), which was clearly confirmed by quantitative analysis of the tubular structures (Figs. S3B–E). Based on in vitro results, the DOBM group was more successful than the OBM, DBM, and DOG-treated groups in inhibiting the generation of HUVECs tubules. The obtained results indicated that DOBM inhibited VEGF expression more strongly than the other groups. This suggests that DOBM suppress tumor cell growth and migration by interacting with VEGF. The concentration of chemotherapeutic medicines in tumor tissues significantly influences the antitumor activity. In the tumor acidic microenvironment, a pH-responsive drug delivery system contributes to providing persistent drug release, prolonging the drug action time, increasing drug concentration, improving the anticancer effect, reducing the systemic drug content and decreasing adverse reactions [51–53]. Therefore, the ability of the BM drug delivery system was evaluated to increase DOX uptake in the tumor by monitoring the residual DOX in tumor tissues. As shown in Fig. 7A–C, the tumor tissues in DBM and DOBM groups showed much higher fluorescence intensities of DOX than the DOG group. There were many poor vascular systems, accompanied by a high extracellular matrix density in tumor tissues. The results suggest that DBM, OBM, and DOBM can overcome these barriers and reach the tumor mass interior. Therefore, BM increased DOX deposition and drug content in tumors by the pH-responsive slow-release drugs, therefore enhancing the inhibitory effect of locally injected therapies on HCC. Tumor cells can change from epithelial into mesenchymal phenotype through EMT, which is a crucial step in tumor cell invasion and metastasis [54]. To further investigate how DOBM inhibited HCC growth and migration, IHC staining was performed on tumor tissues in different groups for E-calmodulin, N-calmodulin, interleukin-6, and TNF-α staining. As shown in Fig. 7D–F, the density of E-calmodulin-positive area was significantly higher and that of the N-calmodulin-positive area of DOBM group significantly decreased relative to the control group, and the difference compared with DOG group was statistically significant. TNF-α and IL-6 are key factors associated with inflammation [55]. IHC analysis (Fig. 7D, G, H) indicated that TNF-α- and IL-6-positive cell percentages were the lowest

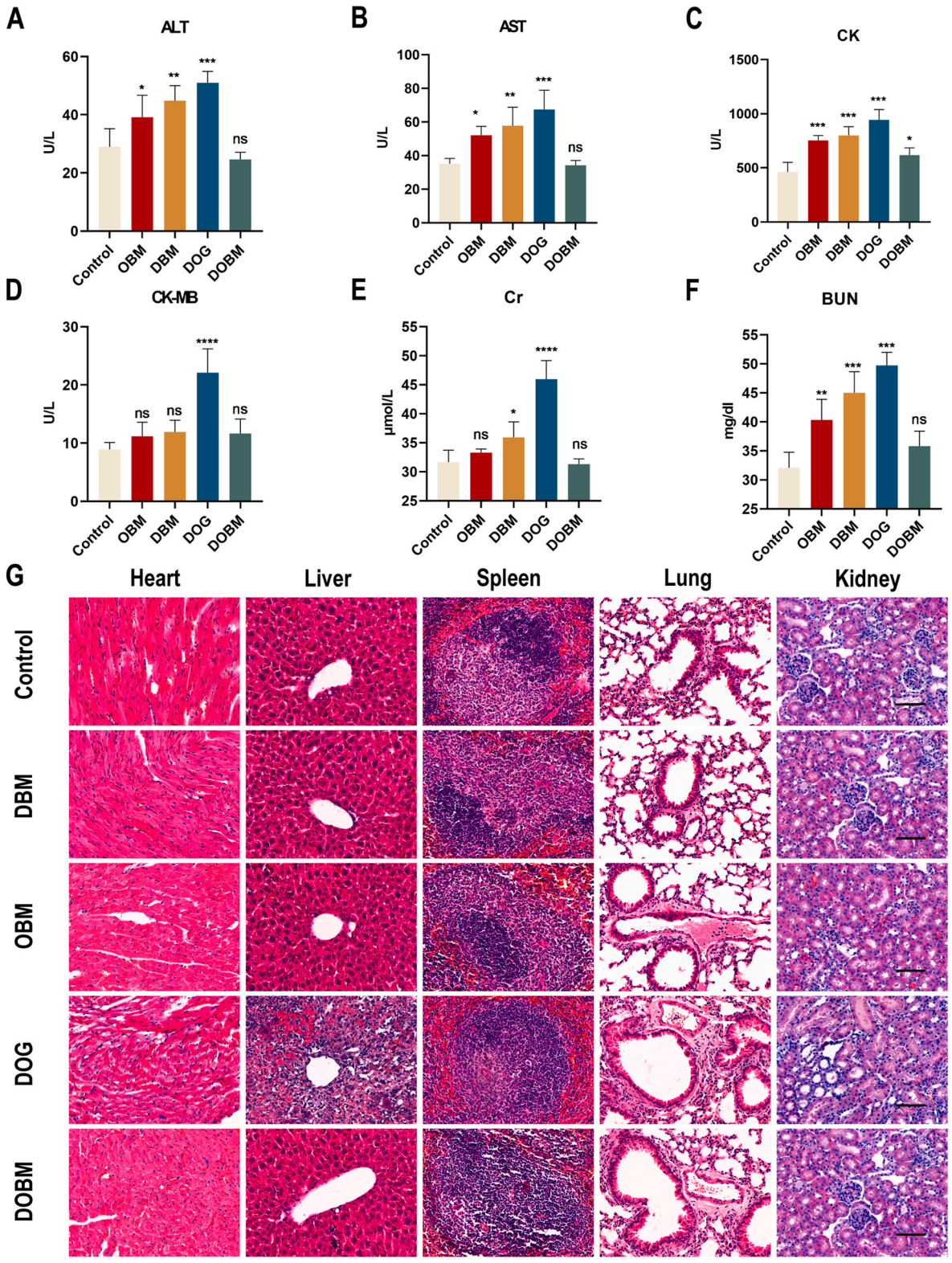

Fig. 8. Biosafety Assessment of DOBM, DBM, OBM, and DOG. (A–F) Changes in hepatic, cardiac, and renal functions of every group. (G) HE staining of liver, heart, lung, spleen, and kidney tissues from every group at 2 weeks of post-treatment. Scale bar: 50 μm.

in the DOBM group. These above results indicate that DOBM slow down the release of DOX and OXA, and inhibit part of the tumor inflammation to inhibit the EMT, thus further suppressing tumor growth and migration.

3.8. *In vivo imaging and the alleviation of harmful side effects*

A real-time fluorescence imaging system was used to examine the in vivo biodistribution of drug-loaded microspheres in tumor-bearing nude mice at different time points after local injection. From Supplementary Fig. S4A, due to the anti-immune clearance and local slow-release

effects, the drug-loaded BSA microsphere groups (OBM, DBM, and DOBM) were slowly released locally in the tumors compared with the direct administration group (DOG), and the fluorescence intensity did not fade significantly within 96 h, while the DOG group showed a weaker fluorescence signal locally in the tumors after 96 h. As displayed in Supplementary Fig. S4B, OBM, DBM and DOBM were mainly distributed in the tumor tissue (Tu). Over time, OBM-, DBM- and DOBM-treated mice showed insignificant signal fading at the tumor site, in comparison with the DOG, where the fluorescence essentially faded completely after 96 h. This may be due to the rapid elimination of blood circulation and the immune system [56]. The above results suggest that localized extended-release therapy with drug-loaded microspheres (OBM, DBM, DOBM) can be maintained for a long period of time compared with the DOG.

The concentrations of DOX and OXA in various mouse samples were calculated using calibration curves. The calibration curves showed sensitive linearity over the concentration range of 0.01–10 μg/mL. The regression equations were $Y = 175.4X + 61.21$ ($R2 = 0.997$) and $Y = 152.1X + 80.80$ ($R2 = 0.997$), respectively. Supplementary Fig. S4C, D present the concentration-time curves for the DOG and DOBM groups. The main pharmacokinetic parameters are shown in Tables 1 and 2. Compared with DOG treatment, DOBM had a significant delayed-release effect, and the T1/2, AUC0-∞ and MRT0-∞ of DOX increased by 398.92 %, 392.96 %, and 478.31 %, respectively, and the Tmax of DOX increased by 30 min. While the T1/2, AUC0-∞ and MRT0-∞ of OXA increased by 369. The results showed the long-lasting and slow-release effect of DOBM, which improves the circulation time of the drug in vivo and enhances the bioavailability of the drug.

The administration of DOX- and OXA-loaded microspheres through local injection to provide sustained-release therapy and minimize the side effects induced by direct chemotherapy can be considered for subsequent clinical applications. After 2 weeks of treatment, the cardiac, hepatic and renal functions, as well as pathological changes in the heart, liver, kidney and spleen were assessed. In the DOG treatment group, ALT and AST levels significantly increased post-treatment, while their levels were not up-regulated in the OBM, DBM, or DOBM treatment group, and their levels slightly increased in the DOBM group relative to the control group (Fig. 8A and B). It may be associated with the necrosis of liver cells and tumor tissues after chemotherapy, causing abnormal renal function. Renal function-related indices, including creatinine and urea nitrogen, increased. The DOG group had significantly increased levels in comparison with other treatment groups, and only a slight increase was observed in the DOBM group (Fig. 8C and D). Myocardial injury-related indices also exhibited corresponding changes. The levels of CK-MB and CK significantly increased only in the DOG group, but not in the DBM, OBM, or DOBM group. The CK levels increased in all groups, with the most pronounced increased being observed in the DOG group (Fig. 8E and F). Histopathological examination based on HE staining indicated significant myocardial injury, renal tubular injury, and hepatic injury in the DOG group, while no pathological change was observed in the other treatment groups, or in the spleen or lungs (Fig. 8G). These results indirectly demonstrate that DOBM have a certain cardio-hepatic and renal protective effect in tumor treatment compared with direct chemotherapy, effectively preventing the formation and recurrence of tumors. This produces a synergistic anti-tumor impact where $1 + 1+1 > 3$. To sum up, DOBM provide vital conversion opportunities and are promising for the treatment of resistant liver cancer.

4. Conclusion

To conclude, in this study, we successfully constructed the BSA dual drug-loading microspheres using TA-$CaCO_3$ as the template. By utilizing the intrinsic properties of BSA, the BM showed efficient dual-drug loading capacity and pH responsiveness, and exhibited the first-fast-then-slow sustained release characteristics for DOX and OXA. DOX and OXA, the two traditional TACE drugs approved locally at a ratio of 1:3, exerted a synergistic effect, which altered the inflammatory factors and ROS levels in the tumor microenvironment with the anti-inflammatory activity of TA component in BM, effectively inhibited tumor growth, recurrence and metastasis, and realized the synergistic antitumor effect. In conclusion, BM exhibit a good biocompatibility and are expected to penetrate the biological barrier, which are promising to be adopted for treating locally advanced refractory HCC with vital clinical translational possibilities.

Funding

This work was Supported by the Major scientific and technological innovation project of Wenzhou Science and Technology Bureau (Grant No. ZY2021009, 2021HZSY0069), Natural Science Foundation of Key-Laboratory of Diagnosis and Treatment of Severe Hepato-PancreaticDiseases of Zhejiang Province (No. G2023004, G2023003). Wenzhou high-level innovation team (Development and application team of functional liver cancer-on-a-chip)

CRediT authorship contribution statement

Jialu Weng: Software, Methodology, Data curation. **Shiyi Wu:** Software, Methodology, Data curation. **Yating Pan:** Software, Methodology, Data curation. **Yifan Lai:** Methodology. **Jinrong Zhu:** Methodology. **Wenzhang Jin:** Methodology. **Deyu Lu:** Conceptualization. **Yizhang Chen:** Supervision, Conceptualization. **Zhijie Yu:** Writing – review & editing, Supervision, Conceptualization. **Xinjie Zan:** Writing – review & editing, Supervision, Conceptualization. **Jinglin Xia:** Writing – review & editing, Supervision, Conceptualization.

Declaration of competing interest

The authors declare the following financial interests/personal relationships which may be considered as potential competing interests: Jinglin xia reports financial support was provided by Major scientific and technological innovation project of Wenzhou Science and Technology Bureau (Grant No. ZY2021009, 2021HZSY0069). Xinjie Zan reports financial support was provided by Natural Science Foundation of KeyLaboratory of Diagnosis and Treatment of Severe Hepato-PancreaticDiseases of Zhejiang Province (No. G2023004, G2023003). Xinjie Zan reports financial support was provided by Wenzhou high-level innovation team (Development and application team of functional liver cancer-on-a-chip). If there are other authors, they declare that they have no known competing financial interests or personal relationships that could have appeared to influence the work reported in this paper.

Appendix A. Supplementary data

Supplementary data to this article can be found online at https://doi.org/10.1016/j.mtbio.2024.101311.

Data availability

Data will be made available on request.

References

[1] EASL clinical practice guidelines: management of hepatocellular carcinoma, Journal of hepatology 69 (1) (2018) 182–236.
[2] N.M. Nader, B.E.-S. Hashem, Epidemiology of hepatocellular carcinoma and intrahepatic cholangiocarcinoma, Cancer Control 24 (3) (2017).
[3] N. Tsuchiya, Y. Sawada, I. Endo, K. Saito, Y. Uemura, T. Nakatsura, Biomarkers for the early diagnosis of hepatocellular carcinoma, World J. Gastroenterol. 21 (37) (2015) 10573–10583.
[4] M.L. Josep, Z.-R. Jessica, P. Eli, S. Bruno, S. Myron, S. Morris, G. Gregory, Hepatocellular carcinoma, Nat Rev Dis Primers 2 (0) (2016).
[5] S.K. Dimitrios, Systemic treatment in intermediate stage (barcelona clinic liver cancer-B) hepatocellular carcinoma, Cancers 16 (1) (2024).

[6] H. Kiyoshi, K. Norihiro, M. Masatoshi, I. Namiki, I. Takafumi, K. Masatoshi, K. Yonson, S. Michiie, N. Osamu, M. Osamu, et al., Comparison of resection and ablation for hepatocellular carcinoma: a cohort study based on a Japanese nationwide survey, J. Hepatol. 58 (4) (2012).
[7] V.J.C. Ravi, Targeted cancer therapy: conferring specificity to cytotoxic drugs, Acc. Chem. Res. 41 (1) (2007).
[8] M. Mary, C. Anne, Recent progress in understanding, diagnosing, and treating hepatocellular carcinoma, CA Cancer J Clin 62 (6) (2012).
[9] I.M. Andrew, F.T. Ian, Drug penetration in solid tumours, Nat. Rev. Cancer 6 (8) (2006).
[10] L. Bin, S. Jing, Z. Junjie, L. Bo, M. Chao, G. Xinquan, L. Kai, Z. Hongjie, W. Fan, S. Juanjuan, et al., Injectable and NIR-responsive DNA-inorganic hybrid hydrogels with outstanding photothermal therapy, Adv Mater 32 (39) (2020).
[11] M. Zhouqi, C. Yu, Z. Xuanfang, L. Chao, L. Jingjing, Z. Rui, C. Liang, Y. Kai, P. Wei, Z. Meifang, et al., Near-infrared-triggered in situ gelation system for repeatedly enhanced photothermal brachytherapy with a single dose, ACS Nano 12 (9) (2018).
[12] A.S. Rahul, M. Ravi, S.H. David, P. Sapna, J.O. Michael, D. Adi, H. Patrick, T. Alda, Assessment of image-guided intratumoral delivery of immunotherapeutics in patients with cancer, JAMA Netw. Open 3 (7) (2020).
[13] Z. Tianru, L. Danna, Z. Qingfei, S. Weijian, S. Xian, Curcumin-encapsulated fish gelatin-based microparticles from microfluidic electrospray for postoperative gastric cancer treatment, Int. J. Biol. Macromol. 254 (0) (2023).
[14] D. Bindu, Anju D. Divtrannum, S. Sapna, An appraisal on various methods of nano particulate formulations, Pharm. Nanotechnol. 5 (4) (2017).
[15] W. Yiming, W. Jie, Y. Zhenyu, H. Haoya, L. Tao, L. Li, G. Xuhong, Chitosan cross-linked poly(acrylic acid) hydrogels: drug release control and mechanism, Colloids Surf. B Biointerfaces 152 (0) (2017).
[16] C. Liu, W. Xi, L. Zhaoyun, L. Ziqi, B. Ziwei, L. Kui, Y. Jian, C. Yuanlu, T. Fei, Metal-organic framework decorated with glycyrrhetinic acid conjugated chitosan as a pH-responsive nanocarrier for targeted drug delivery, Int. J. Biol. Macromol. 240 (0) (2023).
[17] B. Giovanna, M. Lauretta, T. Loredana, L. Rosadele Di, F. Valeria, D.A. Sharon, M. Mariarosa, B. Vittorio, M. Chiara, G. Alessandro, et al., Electrospun fibers as potential carrier systems for enhanced drug release of perphenazine, Int J Pharm 511 (1) (2016).
[18] X. Xinhao, H. Jinyu, X. Huaqian, H. Yingying, L. Ya-Nan, L. Guanyang, L. Liangle, X. Ren-Ai, Applications of human and bovine serum albumins in biomedical engineering: a review, Int. J. Biol. Macromol. 253 (0) (2023).
[19] N. Atanu, L. Sohee, K. Dongjoon, K. Semi, K. Kwang-Sun, Bovine serum albumin-immobilized black phosphorus-based γ-Fe(2)O(3) nanocomposites: a promising biocompatible nanoplatform, Biomedicines 9 (8) (2021).
[20] B. Raluca, S. Daria, G. Luiza, C. Andreea, M. Gabriel, P.-S. Maria, S. Mihaela, M. Dana, F. Monica, A. Simion, Fluorescent phthalocyanine-encapsulated bovine serum albumin nanoparticles: their deployment as therapeutic agents in the NIR region, Molecules 26 (15) (2021).
[21] H. Ying, Y. Jielai, Z. Weiwei, W. Haimang, S. Yulong, C. Yuji, L. Jing, D. Lianfu, X. Xiangyang, C. Wenguo, et al., Biomimetic injectable hydrogel microspheres with enhanced lubrication and controllable drug release for the treatment of osteoarthritis, Bioact. Mater. 6 (10) (2021).
[22] W. Daixu, Q. Ruirui, D. Jinwei, S. Jing, J. Chengmin, W. Xichang, G. Mingyuan, Z. Jian, Soybean lecithin-mediated nanoporous PLGA microspheres with highly entrapped and controlled released BMP-2 as a stem cell platform, Small 14 (22) (2018).
[23] Y. Xiong, L. Chen, P. Liu, T. Yu, C. Lin, C. Yan, Y. Hu, W. Zhou, Y. Sun, A. Panayi, et al., All-in-One: multifunctional hydrogel accelerates oxidative diabetic wound healing through timed-release of exosome and fibroblast growth factor, Small 18 (1) (2022) e2104229.
[24] J. Yan, Y. Wang, M. Ran, R. Mustafa, H. Luo, J. Wang, J. Smått, J. Rosenholm, W. Cui, Y. Lu, et al., Peritumoral microgel reservoir for long-term light-controlled triple-synergistic treatment of osteosarcoma with single ultra-low dose, Small 17 (31) (2021) e2100479.
[25] C. Himanshu, G. Ulrich, A. Deepak, K. Julia, Z. Leilei, B. Marco, G. Tayebeh Mirzaei, S. Ulrich, B. Alexander, Nano-thin walled micro-compartments from transmembrane protein-polymer conjugates, Soft Matter 13 (15) (2017).
[26] Z. Pei, W. Shuang, L. Xiaoman, H. Mohammad, W. Guangyu, H. Xin, Multifunctional and programmable modulated interface reactions on proteinosomes, ACS Appl. Mater. Interfaces 10 (44) (2018).
[27] B. Thomas, J. Anand, A.P. Jasmine, C. Jiwei, J. Yi, C. Catherine, A.A. Thomas, H. C. Stephen, F. Shauna, P. Karline, et al., Low-fouling and biodegradable protein-based particles for thrombus imaging, ACS Nano 12 (7) (2018).
[28] A.K. Mauri, H. Panu, L. Ari, L. Vincent, S. Jani, R. Janne, C. Pierpaolo, Electrostatic assembly of binary nanoparticle superlattices using protein cages, Nat. Nanotechnol. 8 (1) (2012).
[29] M. Damien, T. Pramudana, W. Yajun, G. Tor Kit, B. Anton, C. Frank, Bromoisobutyramide as an intermolecular surface binder for the preparation of free-standing biopolymer assemblies, Adv Mater 23 (47) (2011).
[30] D M C, V D T, Z L, S D, P C, M A M, Q Y, R G, J X, E R J, Structure and formation of highly luminescent protein-stabilized gold clusters, Chem. Sci. 9 (10) (2018).
[31] S A M, S A S, F A, A A, Theranostic magnetite cluster@silica@albumin double-shell particles as suitable carriers for water-insoluble drugs and enhanced T2 MR imaging contrast agents, Mater Sci Eng C Mater Biol Appl 99 (0) (2019).
[32] Z. Qiuhong, C. Jingwen, S. Jie, C. Shixiong, L. Kaicheng, W. Han, C. Hangrong, Inlaying radiosensitizer onto the polypeptide shell of drug-loaded ferritin for imaging and combinational chemo-radiotherapy, Theranostics 9 (10) (2019).
[33] S. Raghu, R. Hadis, P. Sunita, J. Seid Mahdi, Anticancer nano-delivery systems based on bovine serum albumin nanoparticles: a critical review, Int. J. Biol. Macromol. 193 (0) (2021).
[34] J.-E. Ali, R. Leila, J.-E. Rana, T. Mahnaz, A. Ryszard, Latest developments in the detection and separation of bovine serum albumin using molecularly imprinted polymers, Talanta 207 (0) (2019).
[35] W. Jun, Z. Bingbo, Bovine serum albumin as a versatile platform for cancer imaging and therapy, Curr. Med. Chem. 25 (25) (2017).
[36] L. Hoomin, K. Suji, O. Cheolwoo, K. Imran, S. Shruti, K.B. Vivek, H. Young-Kyu, H. Yun Suk, Folic acid-modified bovine serum albumin nanoparticles with doxorubicin and chlorin e6 for effective combinational chemo-photodynamic therapy, Mater Sci Eng C Mater Biol Appl 117 (0) (2020).
[37] L. Zhaoyun, W. Xi, Z. Chen, L. Kui, Y. Jian, Z. Yi, H. Jia, T. Fei, Folic acid-coupled bovine serum albumin-modified magnetic nanocomposites from quantum-sized Fe (3)O(4) and layered double hydroxide for actively targeted delivery of 5-fluorouracil, Int. J. Biol. Macromol. 256 (0) (2023).
[38] P. Arivalagan, E. Thomas Nesakumar Jebakumar Immanuel, V. Bharath Kumar, J. Joe Antony, K. Indira, Toxicity of Doxorubicin (Dox) to different experimental organ systems, Life Sci. 200 (0) (2018).
[39] T. Johnstone, G. Park, S. Lippard, Understanding and improving platinum anticancer drugs–phenanthriplatin, Anticancer research 34 (1) (2014) 471–476.
[40] B. O'Neil, A. Venook, Hepatocellular carcinoma: the role of the north American GI steering committee hepatobiliary task force and the advent of effective drug therapy, Oncol. 12 (12) (2007) 1425–1432.
[41] Y. Winnie, S.M. Tony, Z. Benny, W.T.L. Thomas, B.S.L. Paul, Y.L. Wan, K. Jane, K.F. M. Frankie, C.H.Y. Simon, T.C. Anthony, et al., A randomized phase III study of doxorubicin versus cisplatin/interferon alpha-2b/doxorubicin/fluorouracil (PIAF) combination chemotherapy for unresectable hepatocellular carcinoma, J Natl Cancer Inst 97 (20) (2005).
[42] S. Pengzhong, Q. Jianghui, W. Xiaoxiao, W. Liwen, Z. Tinghong, Y. Dejun, Z. Xingjie, A. Dietmar, A facile and universal method to efficiently fabricate diverse protein capsules for multiple potential applications, ACS Appl. Mater. Interfaces 11 (42) (2019).
[43] Z. Guo, W. Xie, J. Lu, X. Guo, J. Xu, W. Xu, Y. Chi, N. Takuya, H. Wu, L. Zhao, Tannic acid-based metal phenolic networks for bio-applications: a review, J. Mater. Chem. B 9 (20) (2021) 4098–4110.
[44] W. Jing, C. Xiaolan, C. Yu, Q. Feng, Y. Haifeng, Pharmacological effects and mechanisms of tannic acid, Biomedicine & pharmacotherapy = Biomedecine & pharmacotherapie 154 (2022) 113561.
[45] Z. Yanan, T. Chuan, L. Yiming, L. Zaoqu, L. Jing, W. Zijian, H. Xinwei, All-in-one bioactive properties of photothermal nanofibers for accelerating diabetic wound healing, Biomaterials 295 (0) (2023).
[46] T. Chuan, W. Zijian, H. Lei, L. Yimin, W. Kunpeng, L. Zhaonan, H. Bin, J. Dechao, H. Xinwei, Z. Yanan, One-step fabrication of lidocaine/CalliSpheres(®) composites for painless transcatheter arterial embolization, J. Transl. Med. 20 (1) (2022).
[47] A.S. Laura, S.C. Navdeep, Physiological roles of mitochondrial reactive oxygen species, Mol Cell 48 (2) (2012).
[48] W. H, H. B, Damage to DNA by reactive oxygen and nitrogen species: role in inflammatory disease and progression to cancer, Biochem. J. (0) (1996).
[49] V. Marian, L. Dieter, M. Jan, T.D.C. Mark, M. Milan, T. Joshua, Free radicals and antioxidants in normal physiological functions and human disease, Int. J. Biochem. Cell Biol. 39 (1) (2006).
[50] T. Minagawa, K. Yamazaki, Y. Masugi, H. Tsujikawa, H. Ojima, T. Hibi, Y. Abe, H. Yagi, M. Kitago, M. Shinoda, et al., Activation of extracellular signal-regulated kinase is associated with hepatocellular carcinoma with aggressive phenotypes, Hepatol. Res. : the official journal of the Japan Society of Hepatology 50 (3) (2020) 353–364.
[51] S. Wenchuan, L. Kui, Z. Chengyuan, W. Gang, G. Yanyan, L. Li, H. Bin, G. Zhongwei, The potential of self-assembled, pH-responsive nanoparticles of mPEGylated peptide dendron-doxorubicin conjugates for cancer therapy, Biomaterials 34 (5) (2012).
[52] H. Salvador, J.R. Stephan, "The new pH-centric anticancer paradigm in Oncology and Medicine"; SCB, 2017, Semin. Cancer Biol. 43 (0) (2017).
[53] S. Enrico, F. Stefano, Proton pump inhibition and cancer therapeutics: a specific tumor targeting or it is a phenomenon secondary to a systemic buffering? Semin. Cancer Biol. 43 (0) (2017).
[54] X. Ye, Z. Xuefeng, Z. Ruitian, S. Yuening, L. Jian, L. Chengju, Y. Junyi, F. Weiming, G. Qinglong, W. Libin, AFP deletion leads to anti-tumorigenic but pro-metastatic roles in liver cancers with concomitant CTNNB1 mutations, Cancer Lett. 566 (0) (2023).
[55] T. Koji, K. Michael, IL-6 and related cytokines as the critical lynchpins between inflammation and cancer, Semin. Immunol. 26 (1) (2014).
[56] L. Shi-Ying, C. Hong, X. Bo-Ru, Q. Wen-Xiu, Z. Jing-Yue, L. Chu-Xin, W. Shuang-Shuang, Z. Lu, L. Wen-Long, Z. Xian-Zheng, Cancer cell membrane camouflaged cascade bioreactor for cancer targeted starvation and photodynamic therapy, ACS Nano 11 (7) (2017).